

See discussions, stats, and author profiles for this publication at: <https://www.researchgate.net/publication/277895003>

# The effect of particle size on the morphology and thermodynamics of diblock copolymer/tethered-particle membranes

ARTICLE *in* THE JOURNAL OF CHEMICAL PHYSICS · JUNE 2015

Impact Factor: 2.95 · DOI: 10.1063/1.4921961 · Source: PubMed

---

READS

35

## 2 AUTHORS:



Bo Zhang

University of Tennessee

2 PUBLICATIONS 1 CITATION

[SEE PROFILE](#)



Brian J Edwards

University of Tennessee

119 PUBLICATIONS 1,860 CITATIONS

[SEE PROFILE](#)

## The effect of particle size on the morphology and thermodynamics of diblock copolymer/tethered-particle membranes

Bo Zhang and Brian J. Edwards

Citation: *The Journal of Chemical Physics* **142**, 214907 (2015); doi: 10.1063/1.4921961

View online: <http://dx.doi.org/10.1063/1.4921961>

View Table of Contents: <http://scitation.aip.org/content/aip/journal/jcp/142/21?ver=pdfcov>

Published by the AIP Publishing

---

### Articles you may be interested in

**A self-consistent field study of diblock copolymer/charged particle system morphologies for nanofiltration membranes**

*J. Chem. Phys.* **139**, 244909 (2013); 10.1063/1.4851375

**Effect of nanoparticle polydispersity on the self-assembly of polymer tethered nanospheres**

*J. Chem. Phys.* **137**, 104901 (2012); 10.1063/1.4748817

**Strong stretching theory for diblock copolymers in thin films**

*J. Chem. Phys.* **129**, 214903 (2008); 10.1063/1.3027437

**Depletion-induced surface alignment of asymmetric diblock copolymer in selective solvents**

*J. Chem. Phys.* **129**, 044907 (2008); 10.1063/1.2957746

**Fluctuation effects and the stability of the F d d d network phase in diblock copolymer melts**

*J. Chem. Phys.* **128**, 054902 (2008); 10.1063/1.2827472

---

How can you **REACH 100%**  
of researchers at the Top 100  
Physical Sciences Universities?

(TIMES HIGHER EDUCATION RANKINGS, 2014)

With *The Journal of Chemical Physics*.

**AIP** | The Journal of  
Chemical Physics

THERE'S POWER IN NUMBERS. Reach the world with AIP Publishing.



# The effect of particle size on the morphology and thermodynamics of diblock copolymer/tethered-particle membranes

Bo Zhang and Brian J. Edwards<sup>a)</sup>

*Materials Research and Innovation Laboratory (MRAIL), Department of Chemical and Biomolecular Engineering, University of Tennessee, Knoxville, Tennessee 37996, USA*

(Received 16 February 2015; accepted 21 May 2015; published online 5 June 2015)

A combination of self-consistent field theory and density functional theory was used to examine the effect of particle size on the stable, 3-dimensional equilibrium morphologies formed by diblock copolymers with a tethered nanoparticle attached either between the two blocks or at the end of one of the blocks. Particle size was varied between one and four tenths of the radius of gyration of the diblock polymer chain for neutral particles as well as those either favoring or disfavoring segments of the copolymer blocks. Phase diagrams were constructed and analyzed in terms of thermodynamic diagrams to understand the physics associated with the molecular-level self-assembly processes. Typical morphologies were observed, such as lamellar, spheroidal, cylindrical, gyroidal, and perforated lamellar, with the primary concentration region of the tethered particles being influenced heavily by particle size and tethering location, strength of the particle-segment energetic interactions, chain length, and copolymer radius of gyration. The effect of the simulation box size on the observed morphology and system thermodynamics was also investigated, indicating possible effects of confinement upon the system self-assembly processes. © 2015 AIP Publishing LLC. [<http://dx.doi.org/10.1063/1.4921961>]

## I. INTRODUCTION

The design of microporous thin films is an emerging area of technology with great potential to address many outstanding applications in the areas of energy conversion and storage, filtration technology, targeted drug delivery, biosensors, microscale separation processes, etc. For example, the microporous perfluorosulfonic acid membrane Nafion is a well-studied material that has been in use for 50 years by the fuel cell research community in spite of the fact that it has severe limitations in terms of maximum conductance capacity, mechanical and thermal stability, and hydration level.<sup>1–3</sup> The primary reason for the ubiquitous use of Nafion is simply that in all these 50 years, nothing substantially better has been discovered.

Until relatively recently, the development of novel membrane materials has been rate-limited by the process of experimental determination, i.e., the reliance on physical intuition to guide trial-and-error experimentation of potential new membrane materials. This involves lengthy and time consuming chemical syntheses, membrane production, and physical testing. During the past 20 years, however, a combination of experimentation, theory, and simulation has been applied to understanding the key physical principles involved in membrane formation, with the result being a growing body of knowledge regarding the self-assembly of microporous media. Theoretical advances have led to new simulation algorithms as well as adaptation of older techniques, such

as Monte Carlo,<sup>4,5</sup> molecular dynamics,<sup>6,7</sup> dissipative particle dynamics,<sup>8,9</sup> self-consistent field theory (SCFT),<sup>10–12</sup> and hybrid field theory,<sup>13,14</sup> to the study of microporous membrane formation.

Microporous membranes composed of homopolymers with functional side-chains, such as Nafion, are often application-limited by their mechanical and thermal stability, irregular pore microstructure, hydration capacity, and so on. Diblock copolymers, in which the two blocks are composed of mutually immiscible monomeric segments, offer one avenue of progress on account of the wide range of thin film morphologies that can be formed due to the microphase separation that results from the chemical tethering of the blocks.<sup>10–12,15–18</sup> This separation occurs in response to a delicate balance between the enthalpic driving force of the constituent copolymer blocks to phase separate and their inherent entropic driving force to avoid extended chain configurations. A few examples that illustrate the breadth of possible thin-film morphologies are lamellar phases (both parallel and perpendicular to the film width) of alternating blocks, hexagonally packed cylindrical structures formed by one of the copolymer blocks surrounded by a matrix phase of the other block, spheroids of one block surrounded by the other, and more.<sup>10–12,15–21</sup> The key advantages of these diblock membranes over homopolymer derivatives are the regular pore structure and size, as well as the ability to choose the blocks of the copolymer to suit particular applications; i.e., the matrix phase polymer can be chosen to provide thermal or mechanical stability to the membrane and impermeability, whereas the minority phase component can be tuned to the desired physicochemical properties of the membrane. Furthermore, the

<sup>a)</sup>Author to whom correspondence should be addressed. Electronic mail: bje@utk.edu

minority phase polymer can be so chosen such that it can be thermally or chemically degraded without affecting the matrix phase, thus creating a porous network within a mechanically and thermally stable, impermeable thin film.<sup>22,23</sup> The size and surface charge density of these pores can be controlled by a suitable choice of immiscible copolymer blocks and variations of the relative length of each block.

Self-assembly of block copolymers (BCP) with nanoparticles (NP) provides an even more promising means to construct high-performance membranes, since the BCP-NP system can not only self-assemble into an enormous range of interesting nanoscale morphologies<sup>4,5,8,9,13,14,22,24–31</sup> but also allows for the possibility of tailoring the physiochemical properties of the microphase structure to enhance or modify key elements of the membrane functionality, such as conductivity and ionic selection and exclusion. Composites of nanoparticles and copolymers lead to the self-assembly of a diverse array of complex mesophases, depending on factors such as particle size, chemical properties of the particles and blocks, and volume fraction of a given block.<sup>28–31</sup>

In most research carried out to date, the copolymer/nanoparticle systems have been primarily composite systems, i.e., mixtures of particles and the diblock copolymers. Recently, BCP-NP systems have been studied in which the nanoparticles have been chemically tethered to the copolymer.<sup>23,32–35</sup> This incorporates an additional constraint into the self-assembly of membrane morphology since the particle contributions to the free energy of the system help to direct the formation of the microstructure of the material; i.e., the nanoparticles are directly associated with the entropic configurational arrangements of the copolymer block segments, rather than merely energetically (either actively or merely through screening opposite copolymer block segments). In other words, the particles cannot simply be pushed into membrane regions which minimize the energetic interactions between the blocks of the copolymer but must be accommodated in the entropic self-assembly process as part of the copolymer chain. This can result in additional interesting morphologies with more regular patterning (with respect to particle density) than BCP-NP composites without particle/chain tethering.<sup>32–35</sup>

Researchers have studied self-assembled BCP-NP systems for both inorganic (Si and Au) and organic (polyhedral oligomeric silsesquioxane, POSS) molecules.<sup>36,37</sup> The polystyrene-capped gold BCP-NP has been studied in both aqueous and organic media for a wide range of chain lengths. These studies showed that a fairly uniform particle distribution could be produced throughout the film.<sup>37</sup> A block copolymer tethered with POSS can form arrays of cylindrical channels, with radii of approximately 9 nm, by spin coating on a silicon substrate and then exposing to solvent vapor.<sup>23</sup> The location and orientation of nanoparticles within the polymer matrix can also be controlled by their selectivity and size, opening up a wide range of potential applications.<sup>26</sup>

To meet the numerous and demanding technological applications of thin film membranes, it will ultimately be necessary to possess the capability to tailor specific membrane morphologies using theoretical methods and simulations. For example, in nanofiltration membranes, one must be able to

control not only the size of the pores but also their charge (Donnan) exclusion via surface charge density, the latter of which is predominantly controlled by the nanoparticles. Much experimental effort is currently being expended in this area following the intuitive pathways described above, but very little theoretical guidance is available to allow a systematic approach toward future directed membrane self-assembly.

The real-space SCFT is a powerful technique that has proven successful for discovering and predicting morphologies of complex copolymers, both in bulk and in solution. Thompson *et al.* have developed a “self-consistent field theory coupled with density functional theory (SCFT/DFT)” approach that combines self-consistent field theory for the blocks with density functional theory (DFT) for the nanoparticles to examine hybrid composite morphologies.<sup>28,29</sup> Recent theoretical research along these lines has demonstrated that these BCP-NP systems can self-assemble into a variety of interesting morphologies with variable particle distributions concentrated at the interfaces between the distinct polymer-rich regions of the self-assembled structure.<sup>5,13,14,29,30,33</sup> Tethering neutral nanoparticles to one end of the BCP chain directs additional self-assembled structures, including several types of micellar structures, such as rod-like micelles, vesicles, and sphere-like micelles.<sup>14,30–32,34</sup>

Zhu *et al.*<sup>34</sup> performed primarily 2-dimensional simulations of BCP-NP systems with a nanoparticle tethered to one end of the BCP chain. Two cases were studied, one in which the particles were neutral to both blocks of the BCP and one in which the particles disfavored both of the blocks. In cases where a neutral nanoparticle (P) was tethered to the B block of an AB copolymer, three distinct long-range ordered structures were observed. At constant particle radius, when the volume fraction of the A block ( $f_A$ ) was low, the ABP molecules packed into a hexagonal array of A-rich cylinders surrounded by a B-rich matrix, which preferentially contained the majority of the particles. At intermediate values of  $f_A$ , lamellar phases were formed, again with the nanoparticles preferentially located within the B-domains. At high values of  $f_A$ , a narrow region of B-rich cylinders was present, and again the nanoparticles were mostly confined to the B-rich domains (i.e., the cylinders). Changing the particle radius had no effect on the qualitative characteristics of the phase diagram, although increasing particle size tended to narrow the  $f_A$ -range of all three ordered phases. When the interactions of the nanoparticles were unfavorable to both blocks of the copolymer, a wider range of ordered structures was observed, such as morphologies where the particles formed hexagonal arrays of cylindrical domains within a matrix of the AB copolymer and lamellar structures where particle-rich cylinders were located within the B-rich domains.

Zhang *et al.*<sup>35</sup> performed fully 3-dimensional simulations of BCP-NP systems with nanoparticles tethered either at the end of one of the blocks (similarly to Zhu *et al.*<sup>34</sup>) or at the juncture between the two blocks. Five different cases were examined, both for neutral particles and ones that energetically favored or disfavored the segments of one or both blocks. Four morphologies dominated the phase diagrams of the various cases, primarily being the disordered, lamellar, cylindrical, and spheroidal geometries. Depending on the relative lengths

of the blocks, either block could be manipulated into either the matrix or geometric (minority) phase. Furthermore, a semi-precise control over the dimensions of the various geometries could be achieved, such as the cylinder radius and the hexagonal packing dimension of the cylindrical phase. Specific concentrations of the nanoparticles at the interfaces or within the geometric phase could also be achieved via control of the energetic interactions between the nanoparticles and the block segments. Free energy, internal energy, and entropy plots were made for each case, which were then used to rationalize the self-assembled morphology based on chain configuration and energetic interactions between dissimilar chain segments and nanoparticles. All of this behavior was observed for a single diameter particle; i.e., one very important and easily controllable variable was held fixed in these simulations.

The purpose of this article is to extend the suite of simulations performed in the paper of Zhang *et al.*<sup>35</sup> in order to study the effect of particle size in fully 3-dimensional geometries to discern not only the effect of particle size on the observed morphology but also to understand the microscale physics of the self-assembly process in terms of the system free energy, internal energy, and entropy. Similar cases of tethered nanoparticle/copolymer systems are examined as in the previous work using a combination of self-consistent field theory and density functional theory, as described by Thompson *et al.*<sup>28,29</sup> The nanoparticles are allowed to interact (via a standard interaction potential) with either or both blocks of the copolymer, and the stable equilibrium morphologies

are obtained via a suite of 3-dimensional simulations. Phase diagrams of the equilibrium morphologies are constructed, of a similar nature to those of Zhang *et al.*,<sup>35</sup> for several values of the particle radius ( $R_P$ ) ranging from 0.1 to 0.4  $R_g$ , where the symbol  $R_g$  represents the radius of gyration of the diblock copolymer chain. The thermodynamics of the self-assembly process are also evaluated to aid understanding of the configurational interactions that lead to varying morphologies observed in the simulations for the various cases.

## II. SIMULATION METHODOLOGY

We applied the real-space SCFT/DFT<sup>28,29</sup> to simulate the BCP-NP systems studied in this work. In general, a suite of simulations was performed for systems of B-end-tethered (ABP) and center-tethered (APB) particles with ranges of radii ( $R_P \in [0.1, 0.4R_g]$ ), volume fraction of the A segments ( $f_A \in [0.20, 0.80]$ ), and interaction parameters ( $\chi_{APN} = \chi_{BNP} \in [0, 20]$ ), where  $\chi_{iPN}$  is the Flory/Huggins-type interaction parameter between the particles and the  $i$ th block segments multiplied by the chain length, which includes both neutral and strongly interacting particles. Exact details of the systems examined will be described below.

The dimensionless Helmholtz free energy of the system (relative to  $N_C k_B T$ , where  $N_C$  is the number of chains,  $k_B$  is Boltzmann's constant, and  $T$  is the absolute temperature) is expressed as

$$F = -\ln \left( \frac{Q}{V} \right) + \frac{1}{V} \int d\mathbf{r} [\chi_{AB} N \phi_A(\mathbf{r}) \phi_B(\mathbf{r}) + \chi_{AP} N \phi_A(\mathbf{r}) \phi_P(\mathbf{r}) + \chi_{BP} N \phi_B(\mathbf{r}) \phi_P(\mathbf{r}) - w_A(\mathbf{r}) \phi_A(\mathbf{r}) - w_B(\mathbf{r}) \phi_B(\mathbf{r}) - w_P(\mathbf{r}) \rho_P(\mathbf{r}) - \xi(\mathbf{r}) (1 - \phi_A(\mathbf{r}) - \phi_B(\mathbf{r}) - \phi_P(\mathbf{r})) + \rho_P(\mathbf{r}) \psi_{HS}(\bar{\phi}_P(\mathbf{r}))]. \quad (1)$$

In this expression,  $\phi_i(\mathbf{r})$  ( $i = A, B$ , or  $P$ ) is the local volume fraction of the A-block, B-block, or the particles, respectively, and  $\rho_P(\mathbf{r})$  is the particle center distribution.  $\chi_{AB} N$  is the interaction parameter between the A and B block segments of the copolymer. The chain length was set to  $N = 200$  segments. The  $\xi(\mathbf{r})$  is a Lagrange multiplier that is used to ensure that the incompressibility condition is satisfied. The local particle volume fraction,  $\phi_P(\mathbf{r})$ , and weighted nonlocal volume fraction,  $\bar{\phi}_P(\mathbf{r})$ , are calculated as

$$\phi_P(\mathbf{r}) = \frac{1-f}{V_R} \int_{|\mathbf{r}'| < R_P} d\mathbf{r}' \rho_P(\mathbf{r} + \mathbf{r}'), \quad (2)$$

$$\bar{\phi}_P(\mathbf{r}) = \frac{1-f}{V_{2R}} \int_{|\mathbf{r}'| < 2R_P} d\mathbf{r}' \rho_P(\mathbf{r} + \mathbf{r}'). \quad (3)$$

In the above expressions,  $V_R$  and  $V_{2R}$  are the volumes of spheres of radii  $R_P$  and  $2R_P$ , respectively.  $\psi_{HS}$  quantifies the steric repulsion of the particles according to a modified

Carnahan-Starling equation for a hard-sphere fluid,<sup>38</sup>

$$\psi_{HS}(\bar{\phi}_P) = \frac{4\bar{\phi}_P(\mathbf{r}) - 3\bar{\phi}_P(\mathbf{r})^2}{(1 - \bar{\phi}_P(\mathbf{r}))^2}. \quad (4)$$

The hard-sphere fluid described by this equation is rather limited in scope, primarily being limited to solid particles with very little surface flexibility, such as metallic nanoparticles which were investigated in previous work.<sup>34,35</sup> There are other potentials that could be used in a similar treatment, such as potentials for core-shell nanoparticles,<sup>39</sup> but care needs to be exercised for these soft particle systems with respect to the surface integrations, discussed below.

The symbol  $Q$  in Eq. (1) is the system partition function of the entire chain, including the particle, and is defined as

$$Q = \int d\mathbf{r} q(\mathbf{r}, s) q^+(\mathbf{r}, s), \quad (5)$$

where  $q(\mathbf{r}, s)$  and  $q^+(\mathbf{r}, s)$  are the forward and backward propagators of a polymer chain, respectively, which are interpreted

as the probabilities of finding a segment,  $s$ , at position  $\mathbf{r}$ , with the particle viewed as an additional chain segment. This is slightly different than the approach of Ginzburg,<sup>40</sup> who separated the contribution of the grafted particles to the overall partition function since, in that work, the particles were grafted onto oligomeric ligands and not the polymer chains per se. The propagators are introduced according to a Markov process and satisfy the modified diffusion equations<sup>25</sup>

$$\frac{\partial}{\partial s} q(s, \mathbf{r}) = \nabla^2 q(s, \mathbf{r}) - w_i q(s, \mathbf{r}), \quad (6)$$

$$\frac{\partial}{\partial s} q^+(s, \mathbf{r}) = -\nabla^2 q^+(s, \mathbf{r}) + w_i q^+(s, \mathbf{r}). \quad (7)$$

The  $w_i$  in Eqs. (1), (6), and (7) are the self-consistent field potentials of components  $i = A, B, P$ . Denoting the overall volume fraction of the copolymer as  $f$ , the  $w_i$  in Eqs. (6) and (7) is  $w_A$  if  $0 < s < f \cdot f_A$ , and  $w_B$  if  $f \cdot f_A < s < f$ . The overall volume fraction of the particles is determined based on the radius of the particle size being simulated as  $f_P = 0.0009, 0.0079, 0.026$ , and  $0.0602$  for the particle

radii of  $0.1, 0.2, 0.3$ , and  $0.4 R_g$ , respectively. A continuity relationship can then be used to calculate the overall volume fraction of component B:  $f \cdot (f_A + f_B) + f_P = 1$ . The initial condition of Eq. (6) is  $q(0, \mathbf{r}) = 1$  for both the ABP and APB systems, whereas the initial condition of Eq. (7) is  $q^+(0, \mathbf{r}) = \int d\mathbf{n} \exp(-w_p(\mathbf{r} + R_p \mathbf{n}))$  for the ABP system and  $q^+(0, \mathbf{r}) = 1$  for the APB system. Note the implication that the particles are firmly grafted onto the polymer chains; i.e., they are effectively constrained to the role of an additional segment of the overall chain in this work or a ligand in previous work.<sup>40</sup> It is therefore necessary to consider the orientation of the tethering point at the particle surface. The symbol  $\mathbf{n}$  denotes a unit vector, which specifies the direction from the surface of a particle to its adjacent segment of the copolymer chain. A surface integral thus quantifies an orientational probability of the tethering location, as in Eqs. (8c) and (8d).

Minimizing the Helmholtz free energy with respect to the mean fields and densities ( $w_A(\mathbf{r}), w_B(\mathbf{r}), w_P(\mathbf{r}), \phi_A(\mathbf{r}), \phi_B(\mathbf{r}), \rho_P(\mathbf{r})$ , and  $\xi(\mathbf{r})$ ) yields the SCFT/DFT equations,

$$\phi_A(\mathbf{r}) = \frac{V}{Q} \int_0^{f \cdot f_A} ds q(s, \mathbf{r}) q^+(s, \mathbf{r}), \quad (8a)$$

$$\phi_B(\mathbf{r}) = \frac{V}{Q} \int_{f \cdot f_A}^f ds q(s, \mathbf{r}) q^+(s, \mathbf{r}), \quad (8b)$$

$$\rho_P(\mathbf{r}) = \frac{V}{Q} \exp(-w_P(\mathbf{r})) \int d\mathbf{n} q(f, \mathbf{r} + \mathbf{n}R_P), \quad (\text{ABP}) \quad (8c)$$

$$\rho_P(\mathbf{r}) = \frac{V}{Q} \exp(-w_P(\mathbf{r})) \int d\mathbf{n} q(f \cdot f_A, \mathbf{r} + \mathbf{n}R_P) q^+(f \cdot (1 - f_A), \mathbf{r} + \mathbf{n}R_P), \quad (\text{APB}) \quad (8d)$$

$$w_A(\mathbf{r}) = \chi_{AB} N \phi_B(\mathbf{r}) + \chi_{AP} N \phi_P(\mathbf{r}) + \xi(\mathbf{r}), \quad (8e)$$

$$w_B(\mathbf{r}) = \chi_{AB} N \phi_A(\mathbf{r}) + \chi_{BP} N \phi_P(\mathbf{r}) + \xi(\mathbf{r}), \quad (8f)$$

$$w_P(\mathbf{r}) = \psi_{HS}(\bar{\phi}_P(\mathbf{r})) + \frac{1-f}{V_{2R}} \int_{|\mathbf{r}'| < 2R_P} d\mathbf{r}' \rho_P(\mathbf{r}' + \mathbf{r}) \psi'(\bar{\phi}_P(\mathbf{r} + \mathbf{r}'))$$

$$+ \frac{1-f}{V_R} \int_{|\mathbf{r}'| < R_P} d\mathbf{r}' [\chi_{AP} N \phi_A(\mathbf{r}' + \mathbf{r}) + \chi_{BP} N \phi_B(\mathbf{r}' + \mathbf{r}) + \xi(\mathbf{r}' + \mathbf{r})], \quad (8g)$$

$$\phi_A(\mathbf{r}) + \phi_B(\mathbf{r}) + \phi_P(\mathbf{r}) = 1, \quad (8h)$$

where

$$\psi'_{HS}(\bar{\phi}_P) = \frac{d\psi_{HS}(\bar{\phi}_P)}{d\bar{\phi}_P(\mathbf{r})}. \quad (9)$$

The general procedure for solving the SCFT/DFT system of equations was described by Zhang *et al.*<sup>35</sup> Summarizing, simulations were performed in cubic boxes made up of an equivalent number of cubic cells in each direction. In general, the length of each cell dimension was held constant at  $0.109 R_g$ . Thus, the overall simulation volume was varied ranging from  $(3.27R_g)^3$  to  $(5.232R_g)^3$ , which corresponds to

the number of simulation cells ranging from 30 to 48 in each direction. When necessary, the cell dimensions were varied slightly ( $0.109 \pm 0.01R_g$ ) in order to differentiate between different morphologies near their transition points. Each simulation began with setting the initial local values of  $\phi_A(\mathbf{r})$  and  $\phi_B(\mathbf{r})$  using a Gaussian random number generator, whereas  $\rho_P(\mathbf{r})$  was uniform and  $\xi(\mathbf{r})$  was zero at all locations. (In certain cases, a prescribed initial morphological condition was specified to examine closely the free energy differences of local minimum of comparable magnitudes.) Next, the local particle volume fraction,  $\phi_P(\mathbf{r})$ , and weighted nonlocal volume fraction,  $\bar{\phi}_P(\mathbf{r})$ , were calculated via Eqs. (2) and (3),

and the self-consistent field potentials  $w_A(\mathbf{r})$ ,  $w_B(\mathbf{r})$ , and  $w_P(\mathbf{r})$  were obtained from Eqs. (8e)–(8g). The propagators  $q(s, \mathbf{r})$  and  $q^+(s, \mathbf{r})$  could then be solved through diffusion equations, (6) and (7), subject to periodic boundary conditions in the three directions.<sup>41,42</sup> Afterwards, the copolymer chain partition function  $Q$  was calculated according to Eq. (5). The next step evaluated  $\phi_A(\mathbf{r})$ ,  $\phi_B(\mathbf{r})$ ,  $\phi_P(\mathbf{r})$ ,  $\rho_P(\mathbf{r})$ , and  $\bar{\phi}_P(\mathbf{r})$  using Eqs. (8a)–(8d), (2), and (3), respectively. Finally, the potential fields  $w_A(\mathbf{r})$ ,  $w_B(\mathbf{r})$ ,  $w_P(\mathbf{r})$ , and  $\xi(\mathbf{r})$  were updated using the simple mixing method, and the procedure was iterated until the self-consistent field potential differences between two consecutive iterations were smaller than  $10^{-6}$ . The surface integrals in Eqs. (8c) and (8d) were carried out via the mean-value theorem,  $\int f(\mathbf{n})d\mathbf{n} = \bar{f} \cdot S$ , where  $S$  is the area of the surface of integration and  $\bar{f}$  is the mean value of  $f(\mathbf{n})$  over the surface. In the present case,  $f(\mathbf{n})$  is given by the local particle density function. Since a particle center is located at the center of a cell, it was assumed that the surface area of the particle in each adjacent cell had a common value. In this circumstance, an average particle density can be calculated using the simulated value in each cell, which can then be multiplied by the total surface area of the particle,  $4\pi R_p^2$ . This calculation was tested using an independent code that calculated the local particle densities in adjacent cells based on a randomly generated distribution with explicit area counting in each cell. The two methods agreed with each other within 5% of the total area in all cases.

### III. RESULTS AND DISCUSSION

Results of the simulations are presented below in context of four critical areas of practical interest necessary to understand the physical effects of particle size on the self-assembly processes of tethered-particle/block-copolymer systems. The first phenomenon to be examined is the effect of particle size and particle/block interaction strength on the critical point where ordered phase formation first appears as a function of the A-B interaction energy parameter,  $\chi_{AB}N$ . Second, the effect of particle size and particle/block interaction strength on the free energy of the overall system is studied, paying particular attention to its decomposition into energetic and entropic contributions. Next, the variations in the morphological phase diagrams of two systems studied by Zhang *et al.*<sup>35</sup> in response to changes in particle size are discussed, and finally, several technologically important morphologies induced by particles of different sizes are displayed along with their associated density profiles.

#### A. Examination of the critical point for the order/disorder transition

Table I displays the critical points for the disorder/order transition of the morphological phase envelope at  $f_A = 0.5$  for several cases of particle-block interaction parameters,  $\chi_{iPN}$ , where  $i = A, B$ , for both B-end-tethered (ABP) and center-tethered (APB) particle/copolymer systems. The critical point is herein defined as the value of  $\chi_{AB}N$  in each specific case at which the morphology of the system first switches from a disordered phase to an ordered, lamellar microstructure as

$f_A$  is varied over the range [0.2, 0.8]. To obtain a reasonably objective and system-independent quantitative measure of the critical value of  $\chi_{AB}N$ , we employed the somewhat arbitrary criterion that the critical point occurs when the maximum difference of  $\phi_A(\mathbf{r})$  and  $\phi_B(\mathbf{r})$  at any location within the system is greater than 0.3, i.e.,  $\max |\phi_A(\mathbf{r}) - \phi_B(\mathbf{r})| > 0.30$ . This value was chosen based primarily on intuition gained from past experience more than anything else, although we also chose the value 0.3 based on the match between the known values of  $\chi_{AB}N$  (~10.5 to 11.0) for the transition point in the case of a pure A-B block copolymer (i.e., without particles)<sup>43,44</sup> and the (ABP) case of neutral particles ( $\chi_{APN} = \chi_{BPN} = 0$ ) with  $R_p = 0.1R_g$ , which was the smallest value of radius examined herein. For the pure A-B block copolymer, Leibler<sup>43</sup> calculated a value of 10.5 for the transition. This value was confirmed by Fredrickson and Helfand<sup>44</sup> in the mean field limit ( $N \rightarrow \infty$ ), although it increased as  $N$  decreased from the limit of infinite chain length. As it turned out, however, the exact critical point value calculated in this manner was for the most part independent of the value chosen (i.e., 0.3) as long as it fell within the range of  $f_A \in [0.2, 0.8]$ , since  $\phi_A$  and  $\phi_B$  vary strongly near the critical point, producing very steep transition functions.

In the absence of particles, the critical point occurs at  $f_A = 0.5$ , since this corresponds to the highest free energy of interaction based on the maximum in the internal energy which varies as the integral of the term  $\chi_{AB}N\phi_A(\mathbf{r})\phi_B(\mathbf{r})$  and which quantifies the concept that the highest energy state corresponds to the situation which contains the most repulsive interactions, i.e., the case where the number of A and B segments is the same. Keep in mind that although the A and B segments experience repulsive interactions with each other, from a statistical point of view they are equivalent, implying that chain configurational entropy is constant irrespective of the value of  $f_A$  in the disordered phase; e.g., see Figure 2(a) of Zhang *et al.*<sup>35</sup> Consequently, the maximum in the internal energy at  $f_A = 0.5$  determines the exact value of the critical point. It corresponds to the point where the A-B repulsive interactions become large enough to induce a transition to an ordered phase, even though such an occurrence drastically reduces the chain configurational entropy. In the presence of particles, however, the value of  $f_A$  is only approximately 0.5 since the particles contribute to the free energy of the system through the integral of the additional energetic terms  $\chi_{APN}\phi_A(\mathbf{r})\phi_P(\mathbf{r}) + \chi_{BPN}\phi_B(\mathbf{r})\phi_P(\mathbf{r})$  in Eq. (1). In other words, given the continuity expression  $f(f_A + f_B) + f_P = 1$ , the transition point is located in the general neighborhood of  $f_A \approx 0.5$  since  $f_P \ll 1$ .

For the ABP system, four cases were examined: the first (case 1) was  $\chi_{APN} = \chi_{BPN} = 0$ , corresponding to neutral particles. Case 2 was given by  $\chi_{APN} = \chi_{BPN} > 0$ , corresponding to particles disfavoring both A and B segments, as well as cases 3 and 4 where  $\chi_{APN} = -\chi_{BPN} \neq 0$ , in which the value of  $\chi_{APN}$  was both positive and negative, corresponding to particles disfavoring A segments while favoring B segments, and vice versa. In all cases, the absolute value of  $\chi_{APN}$  was varied over the range of [0, 20]. For center-tethered particle chains (APB), only three cases were studied due to the symmetry of the copolymer; hence the case where

TABLE I. The critical points (quantified using the value of  $\chi_{AB}N$  at the disorder/lamellar transition) of the ABP and APB systems at  $f_A = 0.5$ . Error is believed to be less than  $\pm 0.05$ .

$R_P(R_g)$	$\pm\chi_{APN}$	0	5	10	15	20
$\chi_{APN} = \chi_{BPN}$				Critical points of the ABP system		
0.1	$\chi_{APN} = -\chi_{BPN}$	11.0	10.9	10.9	10.9	10.9
	$-\chi_{APN} = \chi_{BPN}$		11.0	11.0	11.0	11.0
	$\chi_{APN} = \chi_{BPN}$		11.1	11.1	11.1	11.1
0.2	$\chi_{APN} = -\chi_{BPN}$	11.1	11.0	10.8	10.7	10.5
	$-\chi_{APN} = \chi_{BPN}$		11.3	11.4	11.6	11.7
	$\chi_{APN} = \chi_{BPN}$		11.5	11.5	11.5	11.5
0.3	$\chi_{APN} = -\chi_{BPN}$	11.5	11.1	10.6	10.1	9.6
	$-\chi_{APN} = \chi_{BPN}$		11.9	12.3	12.7	13.0
	$\chi_{APN} = \chi_{BPN}$		12.1	12.1	12.1	12.0
0.4	$\chi_{APN} = -\chi_{BPN}$	12.2	11.3	10.3	9.1	7.8
	$-\chi_{APN} = \chi_{BPN}$		12.8	13.4	13.8	14.0
$\chi_{APN} = \chi_{BPN}$			Critical points of the APB system			
0.1	$\chi_{APN} = -\chi_{BPN}$	10.9	10.9	10.9	10.9	10.9
	$\chi_{APN} = \chi_{BPN}$		10.9	10.9	10.9	10.9
0.2	$\chi_{APN} = \chi_{BPN}$	11.0	11.0	11.0	11.0	11.0
	$\chi_{APN} = -\chi_{BPN}$		11.0	11.0	11.0	11.0
0.3	$\chi_{APN} = \chi_{BPN}$	11.2	11.2	11.2	11.2	11.2
	$\chi_{APN} = -\chi_{BPN}$		11.2	11.2	11.1	11.0
0.4	$\chi_{APN} = \chi_{BPN}$	11.7	11.6	11.6	11.6	11.6
	$\chi_{APN} = -\chi_{BPN}$		11.6	11.4	11.0	10.6

$\chi_{APN}$  assumed negative values was physically equivalent to the one in which it was always positive.

### 1. End-tethered particle/copolymer systems

Case 1: From Table I, it is evident that the critical point of the B-end-tethered neutral particle system (case 1:  $\chi_{APN} = \chi_{BPN} = 0$ ) is a strong function of particle radius, increasing from a value of 11.0 for  $R_P = 0.1R_g$  to 12.2 for  $R_P = 0.4R_g$ . One must keep in mind that the stable, equilibrium morphology of the system is determined by the global minimum in free energy with respect to each possible microphase. Whereas the free energy is the sum of two contributions, i.e., the internal energy and the entropy ( $F = U - TS$ ), the transition from the disordered phase to the ordered, lamellar structure is dictated by a complex balance between these two contributions. The internal energy contribution to  $F$  is given by the integral of the first three terms of the integrand on the right side of Eq. (1),  $\chi_{AB}N\phi_A(\mathbf{r})\phi_B(\mathbf{r}) + \chi_{APN}\phi_A(\mathbf{r})\phi_P(\mathbf{r}) + \chi_{BPN}\phi_B(\mathbf{r})\phi_P(\mathbf{r})$ , whereas the entropic contribution is constituted of all the remaining terms in Eq. (1). Since it is universally true that  $\phi_P \ll 1$ ,  $\phi_B \approx 1 - \phi_A$ , the integrand of the energetic contribution to the free energy can be expressed as approximately equal to  $\chi_{AB}N\phi_A(1 - \phi_A) + \chi_{APN}\phi_A\phi_P + \chi_{BPN}(1 - \phi_A)\phi_P$ . For neutral particles, only the first of these terms is nonzero, and in the disordered phase,  $\phi_A$  tends to values in the middle of its range of [0, 1] because the entropic contribution dominates the free energy, even though the internal energy attains its maximum value at about

$\phi_A \approx 0.5$ . As  $\chi_{AB}N$  increases, the internal energy within the disordered phase increases proportionally, driving up the free energy even though the entropic contribution still dictates the stable (disordered) morphology and changes little with increasing  $\chi_{AB}N$ . Nevertheless, given the inverted parabolic form of the internal energy contribution ( $\chi_{AB}N\phi_A[1 - \phi_A]$ ), eventually the free energy of the system can be lowered by driving  $\phi_A$  toward the fringes of its range, causing an abrupt, dramatic decrease in the internal energy, and hence initiating a phase separation to a more ordered phase, even though this results in a substantial decrease in the configurational entropy of the system. [The reader can visualize the above arguments with reference to Fig. 2.]

With no intrinsic preference for A or B segments ( $\chi_{APN} = \chi_{BPN} = 0$ ), neutral particles contribute directly only to the entropic part of the free energy, although they indirectly influence the internal energy by locally affecting the value of  $\phi_A$ . Hence when the neutral particles are relatively small, they do not greatly influence the system configurational entropy or internal energy, and values of  $\chi_{AB}N$  at the critical point are approximately the same (10.5–11.0) as in the case of a pure A-B block copolymer.<sup>43–45</sup> As particle size becomes significant, however, the particles influence the entropic contribution to the free energy by increasing the effective nonlocal particle volume fraction,  $\bar{\phi}_P$ , according to the Carnahan-Starling expression in Eq. (1),  $(4\bar{\phi}_P - 3\bar{\phi}_P^2)/(1 - \bar{\phi})^2$ . Hence, increasing particle size, which effectively increases  $\bar{\phi}_P$ , results in a corresponding increase in the configurational entropy of the system. Although A and B segments are statistically

equivalent, they are not statistically equivalent to the particles, and hence increasing particle volume fraction results in an increase of the entropic contribution to the free energy. As a consequence, the energetic repulsive interactions of the A and B segments must be stronger as  $R_P$  increases in order to overcome the additional entropic penalty associated with forcing the chains into an ordered state.

For the most part, the neutral particles generally concentrate within the B-rich domains since they are tethered to the B-end of the block copolymer. However, in some circumstances, the neutral particles will preferentially occupy sites that tend to screen the repulsive A and B segments from each other at the interfaces of the A-rich and B-rich domains, thereby effectively lowering the internal energy contribution to the free energy. As a consequence, a greater value of  $\chi_{AB}N$  is required to reduce the mitigating screening effect of the particles in order to drive the system into an ordered phase. As the particles increase in size, their screening potential becomes higher, and thus it requires a greater degree of repulsion between the A and B segments to initiate a microphase separation. Therefore, in these circumstances, this additional screening mechanism can play an important role in determining the relative concentrations of the particles within and at the interfaces of the A-rich and B-rich domains.

Case 2: Irrespective of particle size, when the particles are equally repulsive to both A and B segments, the effect of increasing  $\chi_{iPN}$  is negligible. When  $\chi_{iPN} < \chi_{AB}N$ , the particles can still act as screens, although less effectively, between the more repulsive A and B segments. However, once  $\chi_{iPN} > \chi_{AB}N$ , the driving force toward particle screening between the A and B segments is removed, resulting in a lower entropically induced increase in  $F$ , and therefore one might expect to observe an associated decrease of the critical value of  $\chi_{AB}N$ . This is due to the fact that the particle no longer has a screening effect when it is highly repulsive to both blocks, and as such it merely acts as an additional segment attached to the end of the B chain, which does not affect the configurational state of the polymer chain to

as great of a degree as it does when the particle prefers to locate between the highly repulsive A and B segments, regardless of the magnitude of  $\chi_{iPN}$ . Nevertheless, the overall effect of repulsive particles to both A and B segments is to lower the critical value of  $\chi_{AB}N$  necessary to induce a morphological phase transition from a disordered state to an ordered one, although this trend is very slight given that the contributions of  $\chi_{iPN}$  to the free energy are quite small in that the energetic term,  $\chi_{AB}N\phi_A(1 - \phi_A) + \chi_{APN}\phi_A\phi_P + \chi_{BPN}(1 - \phi_A)\phi_P$ , is relatively unchanged since  $\phi_P \ll 1$ . Consequently, such a trend is only barely noticeable in the data of Table I for the largest particle radius,  $R_P = 0.4R_g$ , where the slight additional contribution of the particles to the internal energy effectively lowers the necessary degree of repulsion (quantified by  $\chi_{AB}N$ ) to initiate a transition to an ordered morphology.

Although there appears to be little effect on the value of the critical point, increasing the particle/block interaction parameters when  $\chi_{APN} = \chi_{BPN} > 0$  induces a slight but definite increase in the degree of segregation between the A-rich and B-rich domains, as displayed in Figure 1 for the case of  $R_P = 0.2R_g$ . This appears to be a consequence of the slight but increasing contribution to the internal energy of the particle density distribution,  $\chi_{APN}\phi_A\phi_P + \chi_{BPN}(1 - \phi_A)\phi_P$ , and hence to the overall system free energy, which effectively pushes the phase separating ordered morphology slightly further toward the fringes of the  $\phi_A$  range [0, 1].

Case 3: The next case corresponds to the situation where the particles disfavor the A segments and favor the B segments, i.e.,  $\chi_{APN} > 0$  and  $\chi_{BPN} < 0$ . In this case, there is a generally strong decrease in the critical value of  $\chi_{AB}N$  affected by the increasing magnitude of  $\chi_{APN} = -\chi_{BPN}$ , which grows stronger as particle size is increased—see Table I. At the smallest particle radius,  $R_P = 0.1R_g$ , the effect is only slight. This is a consequence of the small reduction in the internal energy due to the presence of the particles, not only since  $\phi_P \ll 1$  but also since the contributions of the two particle terms to the internal energy have opposite signs and

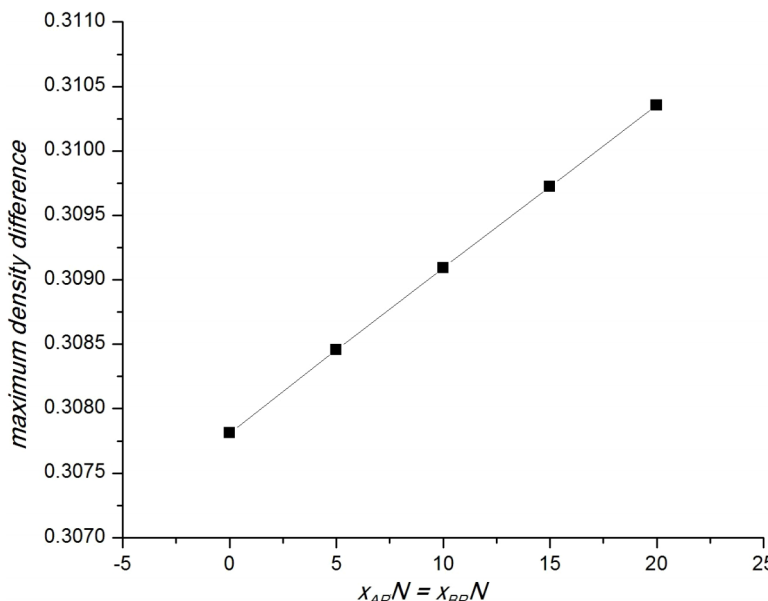


FIG. 1. The maximum density difference ( $\max |\phi_A - \phi_B|$ ) as a function of the particle/block interaction parameters  $\chi_{APN} = \chi_{BPN}$  at  $R_P = 0.2R_g$  and  $\chi_{AB}N = 11.1$  in the ABP system.

tend to cancel each other since  $\chi_{APN} = -\chi_{BPN}$ . The net effect is to lower the value of  $\chi_{ABN}$  necessary to achieve the ordered phase formation. With regard to the entropy, since the particles are attached to the end of the B block, which they favor, there is no driving force to induce a major configurational rearrangement in which the particles encroach upon the A block, which the particles disfavor. Consequently, the situation for particles of size  $R_P = 0.1R_g$  is very similar to the case of particles which are repulsive to both A and B segments, with similar quantitative values of the critical point between these two cases. As particle size increases, the critical point likewise increases due to the increase in  $\phi_P$  manifesting through the Carnahan-Starling excluded volume potential; i.e., the entropy grows commensurately with particle size, as discussed previously.

For larger particle radii, the decreasing trend with increasing particle interaction strength becomes more significant—see Table I. This is primarily caused by a dramatic decrease in the internal energy with ordered phase formation since the particles are highly motivated to congregate in the B-rich domains of the overall system. The driving force is thus the tendency of the particles to migrate away from A segments and surround themselves with B segments. Consequently, the internal energy contribution to the free energy,  $\chi_{ABN}\phi_A(\mathbf{r})\phi_B(\mathbf{r}) + \chi_{APN}\phi_A(\mathbf{r})\phi_P(\mathbf{r}) + \chi_{BPN}\phi_B(\mathbf{r})\phi_P(\mathbf{r})$ , dominates the free energy. In the disordered state, where the particles are more evenly distributed throughout the domain, the final two terms in the above expression tend to cancel themselves out due to the difference in signs of the interaction parameters,  $\chi_{APN} = -\chi_{BPN}$ . In the ordered state,  $\phi_P$  concentrates in the B-rich regions and is relatively depleted in the A-rich regions, and hence the magnitude of the third term is significantly greater than that of the second. Since the third term involves an attractive interaction parameter (i.e., it is negative), its net effect is to lower the internal energy of the system and thereby to induce an ordered phase formation at a lower value of the critical point than would otherwise occur. This trend increases dramatically with increasing particle/block interaction strength, resulting in the substantial decrease in the critical point within increasing  $\chi_{APN} = -\chi_{BPN}$  at constant particle radius, as observed in Table I.

Case 4: The final case of the ABP system corresponds to the situation in which the particles favor the A segments and disfavor the B segments, i.e.,  $\chi_{APN} < 0$  and  $\chi_{BPN} > 0$ . As the magnitude of  $\chi_{APN}$  increases, the effect on the critical point is extremely pronounced, showing a substantial increase in the value of  $\chi_{ABN}$ . This dramatic rise is due to the weighting of the relative effects of entropy and internal energy on the free energy. Due to the mismatch in the signs of  $\chi_{APN}$  and  $\chi_{BPN}$ , the particles tend to migrate to regions of high A segment concentrations, distorting the B-block chain configurations into low entropy states, and hence driving up the free energy. However, since the particles are repulsive to B segments, they are not effective at screening the A and B segments from each other, as in the case of neutral particles. Indeed, for higher magnitudes of  $\chi_{APN}$ , the particles are actually concentrated within the A-rich domains, and A segments occupy interfacial locations

with the B segments since the repulsion between A and B segments is weaker than the repulsion between B segments and the particles. This imparts even greater configurational contortions to the B-blocks of the chains, thus driving down the entropy and increasing the free energy of the disordered state. Furthermore, since the internal energy expression scales with particle interaction strength as  $\chi_{ABN}\phi_A(\mathbf{r})\phi_B(\mathbf{r}) + \chi_{APN}\phi_A(\mathbf{r})\phi_P(\mathbf{r}) + \chi_{BPN}\phi_B(\mathbf{r})\phi_P(\mathbf{r})$ , there is a strong positive contribution to the free energy resulting from the relatively high magnitude of the second (positive) term with respect to the third (negative) term. On account of this, a higher absolute value of  $\chi_{ABN}$  is required to drive the system to the ordered state to overcome the entropic penalty of forcing the particles into a configurationally unfavorable state.

## 2. Center-tethered particle/copolymer systems

Case 1: The center-tethered particle/copolymer system with neutral particles exhibited the same qualitative behavior as the end-tethered system; i.e., the critical value of  $\chi_{ABN}$  at the disorder/order transition increased with particle radius, as displayed in Table I. As in the ABP system, there was only a slight effect at small particle radii, which was due to the low configurational entropic penalty induced by the presence of the particles. For larger particle radii, where the impact of the particles on the internal energy was more severe, again the effect on the critical point was more substantial, but for each value of particle radius, the cumulative effect was smaller for the center-tethered particle system than the end-tethered one. For example, at  $R_P = 0.4R_g$ , the critical point of the ABP system occurred at  $\chi_{ABN} = 12.2$ , whereas it occurred at 11.7 for the APB system—see Table I. This is a direct consequence of the tethering position: for the center-tethered system, the neutral particle was already located at a point in the chain where it could induce maximal screening between the repulsive A and B segments, without causing a substantial decrease in the configurational entropy of the B block, as required in the ABP system. Consequently, the entropic penalty imparted to the free energy imposed a significantly lower entropically induced increase in  $F$  in the APB system than in the ABP, hence requiring a smaller energetic contribution from  $\chi_{ABN}$  in the APB system relative to the pure copolymer case to induce the morphological phase transition from a disordered state to an ordered one.

Case 2: When the particles disfavor both blocks equally ( $\chi_{APN} = \chi_{BPN} > 0$ ), there is practically no effect of particle interactions on the critical point irrespective of the magnitude of the specific value of  $\chi_{APN}$ . Since the particle is located at the center of the chain, once again the decrease in the configurational entropy of the APB system is very slight relative to that in the ABP system. The particles tend to concentrate at the interfaces between the A-rich and B-rich domains, as one might expect from their tethering location, essentially screening the A segments from the B segments. However, since the particles are equally repulsive to both types of segments, there is no impetus for the particles to change location as  $\chi_{APN}$  is increased, implying that this quantity has little effect on the configurational entropy. Furthermore, whereas the contributions of the particle/block

interaction parameters to the internal energy are very small (since  $\phi_P \ll 1$ ), there is not much difference in the free energy from one value of  $\chi_{APN}$  to the next. Therefore, even at the largest particle radius, only a slight effect is barely discernible in Table I.

Case 3: In the third case, where particles disfavor the A segments and favor the B segments (i.e.,  $\chi_{APN} > 0$  and  $\chi_{BPN} < 0$ ), there is essentially no discernible effect of increasing  $\chi_{APN}$  on the critical point except for the largest particle radius,  $R_P = 0.4R_g$ . This is primarily a result of the tethering location, which tends under most conditions to concentrate the particles at the interface, rather than within domains of A-rich or B-rich phases. Consequently, with  $\phi_P$  more spatially uniform (with respect to the A-rich and B-rich domains), the opposite signs in the particle contributions to the internal energy (i.e.,  $\chi_{APN} = -\chi_{BPN}$ ) tend to cancel each other out, thereby mitigating any potential impact on the free energy of the overall system.

In the case of  $R_P = 0.4R_g$ , the trend is one of decreasing values of  $\chi_{ABN}$  at the critical point as the particle/block interaction parameters increase in magnitude. Even though the particles always remain concentrated at the interfaces between the A-rich and B-rich domains on account of their tethering location, the increasing repulsion/attraction between the particles and A/B segments tends to shift their concentration increasingly toward the B-rich interfacial region as  $\chi_{APN}$  ( $= -\chi_{BPN}$ ) increases. Hence, there is a slight configurational entropic penalty that affects the critical point as the particles are pulled deeper into the B-rich domain by their attractive interactions with the B segments and repulsive interactions with the A segments. Furthermore, the internal energy decreases since the negative B-P interaction term in the internal energy expression becomes increasingly significant relative to the A-P interaction term. The net result is the decreasing trend in the critical point with increasing  $\chi_{APN}$ , as evident in Table I, since a lower value of  $\chi_{ABN}$  is required to initiate a phase separation into an ordered phase.

## B. Thermodynamics of tethered particle/block copolymer systems

The effects of the tethered particles on the overall system thermodynamics can be assessed by examining the relative changes in the free energy, internal energy, and entropy in response to variations of particle size and interaction strength. In the following discussion, we examine only neutral particle ABP and APB systems ( $\chi_{APN} = \chi_{BPN} = 0$ ), since similar diagrams and arguments to those described below apply to the other cases discussed in Subsection III A. In Figure 2, plots of  $\Delta F$ ,  $\Delta U$ , and  $-\Delta TS$  are displayed as functions of  $f_A \in [0.2, 0.8]$  for the ABP and APB systems.  $U$  and  $\Delta TS$  are rendered dimensionless in the same fashion as  $\Delta F$ , i.e., with respect to  $N_c k_B T$ . Values of the entropy change are calculated with reference to the value of  $TS$  for the  $R_P = 0.1R_g$  particles at  $f_A = 0.2$ ; hence, the value of  $-\Delta TS = 0$  for the  $R_P = 0.1R_g$  curve at the point  $f_A = 0.2$  in Figs. 2(e) and 2(f). This then translates into appropriate relative reference points for  $\Delta F$  and  $\Delta U$  that are determined from the Legendre transformation

$\Delta F = \Delta U - \Delta TS$ . The value of the A-B interaction parameter is held constant in the following discussion at  $\chi_{ABN} = 18$  since this value is known to produce a wide variety of morphologies, dependent on the particular value of  $f_A$  under consideration.<sup>34,35</sup> Note that the global maxima in the  $\Delta F$  curves and the global minima in the  $\Delta U$  curves do not occur exactly at  $f_A = 0.5$  due to the small but finite effect of the particles. Also note that the three panels of the APB systems, Figs. 2(b), 2(d), and 2(f), only cover the range of  $f_A \in [0.2, 0.5]$  since the curves are symmetric due to the center-tethered particle location.

### 1. Effect of particle size

a. ABP system. The effects of the tethered particles on the overall system thermodynamics can be assessed by examining the relative changes in the free energy, internal energy, and entropy in response to variations of particle size and interaction strength. First, we will examine the thermodynamics of the ABP tethered-particle/copolymer system. From Fig. 2(e), it is evident that  $-\Delta TS$  is constant at both low and high values of  $f_A$  (i.e.,  $0.275 < f_A > 0.75$ ), regardless of particle size. This is because of the statistical equivalence of the A and B segments, as discussed in Sec. III A 1: since the A and B segments are statistically indistinguishable from each other, there is no entropy of mixing effect upon the system as  $f_A$  is varied. The entropy increases with increasing particle size in Fig. 2(e), which is due to the Carnahan-Starling form of the excluded volume potential,  $(4\bar{\phi}_P - 3\bar{\phi}_P^2)/(1 - \bar{\phi})^2$ , which is an increasing function of particle size since  $\bar{\phi}_P$  scales with  $R_P$ . Hence the particles, which are not statistically equivalent with the A and B segments, increase the system configurational entropy by augmenting the final term in the continuity equation  $f(f_A + f_B) + f_P = 1$ , thereby introducing an entropy of mixing effect into the system. When  $f_A \in [0.3, 0.725]$ , the entropy experiences a sharp decrease on account of the transition to one of the several well-known ordered phases (lamellar, cylindrical, spheroidal, etc.), depending on the particular value of  $f_A$ . This is caused by the packing frustration experienced by the chains as they experience configurational changes to accommodate the ordered phase formation. The entropy change exhibits a minimum at  $f_A \approx 0.5$ , which is due to the increasing degree of order imparted to the system as the number of A and B segmental interactions (with strength  $\chi_{ABN}$ ) is maximized because the number of A and B segments is approximately equal at this value of  $f_A$ .

In the range of  $0.275 < f_A > 0.75$ , the internal energy of the ABP system changes dramatically, as evident in Fig. 2(c), increasing at low  $f_A$  and decreasing at high  $f_A$ . This is caused by the increasing number of A-B interactions in the disordered phase and the relative numbers of A and B segments as  $f_A$  increases (at low values of  $f_A$ ), thereby influencing the overall strength of the repulsive A-B interactions. However, in the range of  $f_A \in [0.3, 0.725]$ , the internal energy experiences an abrupt, significant decrease as the ordered phases are formed, which greatly reduce the number and strength of A-B interactions. A minimum is thus evident at  $f_A \approx 0.5$ , even though in principle one would intuitively expect a stronger

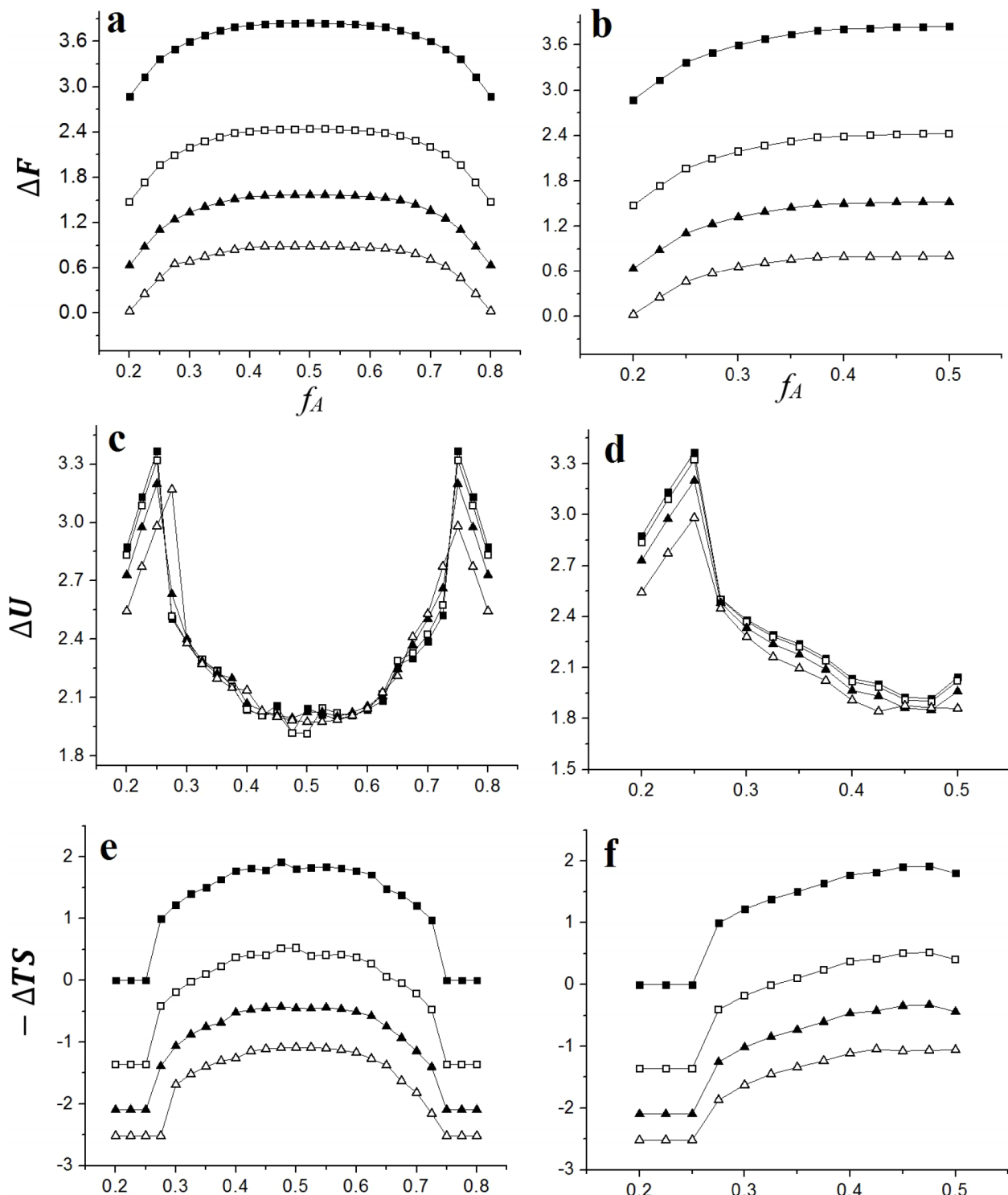


FIG. 2. Key thermodynamic quantities as functions of  $f_A$  for neutral particles of varying radii at  $\chi_{AB}N = 18$ . The left column is the ABP system and the right column is the APB system. Symbols denote particles of a certain radius as follows: ■ ( $0.1R_g$ ), □ ( $0.2R_g$ ), ▲ ( $0.3R_g$ ), and △ ( $0.4R_g$ ). Panels (a) and (b) depict the free energy change ( $\Delta F$ ), (c) and (d) show the internal energy change ( $\Delta U$ ), and (e) and (f) display the entropic change ( $-\Delta TS$ ).

A-B overall interaction energy (i.e., a maximum) due to the equal number of A and B segments; however, the increase in the degree of ordering more than offsets this effect. As particle size increases, there is a significant drop in the internal energy change, which is a result of the fact that larger particles more effectively screen the A and B segments from each other. Mathematically speaking, for neutral particles,

$\chi_{AP}N = \chi_{BP}N = 0$ , which implies that the internal energy varies as  $\chi_{AB}N\phi_A\phi_B$ ; i.e.,  $\phi_A$  and  $\phi_B$  decrease slightly on average as particle size, and hence  $\phi_P$ , increases due to the incompressibility condition. An interesting observation taken from Fig. 2(c) is that there does not appear to be much effect of particle size on the internal energy change inside the ordered-phase regime of the ABP system when  $f_A \in [0.3, 0.725]$ . This

can partially be explained by considering the tethering location of the particles. Since the particles are tethered to the B-end of the block copolymer chain, as the degree of order increases, the particles are effectively confined to the B-rich domains by the entropic chain packing frustration, thereby effectively reducing the screening effect between A and B segments at the interfaces of the A-rich and B-rich domains. Since the interfaces are relatively depleted of particles, the local particle volume fraction,  $\phi_P$ , in these regions is very small and hence does not affect the internal energy,  $\chi_{AB}N\phi_A\phi_B$ , to an appreciable degree.

The free energy change within the ABP system is quantified by the difference in the internal energy and entropy changes through the Legendre transformation  $\Delta F = \Delta U - \Delta TS$ . In the disordered state, when  $0.275 < f_A > 0.75$ , the free energy rises rapidly as  $f_A$  increases or decreases from the extremes of its range. Here, the free energy change is identical with the change in the internal energy, since the change in the entropic contribution to  $\Delta F$  is zero—see panel (e) of Fig. 2. Hence, a sharp parabolic profile is observed, as expected from the mathematical form of  $U = \chi_{AB}N\phi_A\phi_B \approx \chi_{AB}N\phi_A(1 - \phi_A)$ . When  $f_A \in [0.3, 0.725]$ ,  $\Delta F$  flattens off to a maximum at  $f_A \approx 0.5$  in the ordered phase regime, since the sharp parabolic form of the internal energy is damped by the decrease in the entropic contribution to the free energy. This flatness of  $\Delta F$  in the ordered-phase region indicates only slight free energy differences between the various ordered-phase morphologies appearing within this range of  $f_A$  values. As the particle size increases,  $\Delta F$  decreases, with the primary determinant being the entropic contribution, since the internal energy does not change substantially with particle radius, as discussed above.

*b. APB system.* The thermodynamics of the APB system are very similar to those of the ABP system, with the minor exception of the internal energy change, which exhibits a distinct trend with respect to variable particle radius; i.e., within the ordered-phase regime of  $f_A \in [0.3, 0.725]$ , the internal energy decreases as particle size increases, as displayed in Fig. 2(d). The reason for this is related to the tethering position of the particle, directly between the A and B blocks of the particle chain. At this location, the particles are always at positions near to the interfaces of the A-rich and B-rich domains where they can effectively screen the A and B segments from each other, thereby reducing the A and B net repulsive energy in the system. The mitigating effects of this screening are felt more substantially for the larger particles, which create a more effective blocking network between the A and B segments. From a mathematical perspective, the local particle concentrations,  $\phi_P$ , at the interfaces are relatively higher with respect to the ABP system, and hence the interfacial internal energy change,  $U = \chi_{AB}N\phi_A\phi_B$ , decreases significantly with particle size since  $\phi_A$  and  $\phi_B$  at the interfaces are substantially smaller than in the ABP case.

## 2. Effect of particle/block energetic interactions

The effects of the particle/block interaction potential upon the thermodynamic properties of the system are presented in

Fig. 3 for the ABP and APB systems for particles that disfavor both blocks of the copolymer chain, i.e.,  $\chi_{APN} = \chi_{BPN} \equiv \chi_{A/BPN} \geq 0$ . The value of the A-B interaction parameter,  $\chi_{AB}N$ , is once again set at the value 18, whereas the particle block interaction parameters vary over the range [0, 15]. The reference state is the same as in Fig. 2: all quantities are calculated relative to the value of entropic contribution to the free energy at  $R_P = 0.1R_g$ ,  $f_A = 0.2$ , and  $\chi_{A/BPN} = 0$ . Once again, the APB profiles are symmetric around the corresponding maximum in each curve, such that only the limited range of  $f_A \in [0.2, 0.5]$  is presented in panels (b), (d), and (f) of Fig. 3.

In the case of interacting particles, the behavior of the thermodynamic functions with respect to particle/block interaction energy is essentially independent of the tethering point of the particle along the chain backbone. Hence, the ABP and APB systems can be discussed collectively, with only small quantitative discrepancies between the two cases. The entropic contributions to the free energy are independent of the interaction potential, as would be expected, since these are not direct functions of  $\chi_{A/BPN}$ . Since the particles are equally repulsive to both types of segments, the statistical configurational state of the chains is unaffected by the particle/segment interaction strength. In other words, the maximum entropy configurational state is the same as for the neutral particle case, implying equivalent morphologies for any particular value of  $\chi_{AB}N$ . (We shall see an interesting consequence of this observation in Sec. III C.) The internal energy changes slightly with particle/block interaction strength, increasing with  $\chi_{A/BPN}$ . This is the expected consequence of the energetic expression  $\chi_{AB}N\phi_A(1 - \phi_A) + \chi_{APN}\phi_A\phi_P + \chi_{BPN}(1 - \phi_A)\phi_P$ , which grows stronger as  $\chi_{A/BPN}$  increases. This directly impacts the free energy change within the system, producing an inverted parabolic profile for  $\Delta F$  that grows sharper with increasing  $\chi_{A/BPN}$ . The  $\Delta F$  profiles in Figs. 3(a) and 3(b) tend to flatten out in the middle of the  $f_A$  range, indicating fairly similar free energy values of the various ordered phases that appear in this region of the phase diagram.

## C. Particle size effect on the morphology of tethered-particle/block-copolymer systems

Morphological phase diagrams for several cases of ABP and APB tethered-particle/copolymer systems were presented by Zhu *et al.*<sup>34</sup> and Zhang *et al.*<sup>35</sup> The effect of particle size on the phase diagrams is discussed below with reference to the neutral particle ( $\chi_{A/BPN} = 0$ ) ABP and APB systems at  $\chi_{AB}N = 18$ , since these phase diagrams are representative of those found in the other cases discussed in Secs. III A and III B. Phase diagrams (in  $R_P - f_A$  space) for these two cases are presented in Fig. 4. The APB phase diagram is symmetric about the point  $f_A \approx 0.5$  due to the centralized tethering position of the particles between the two blocks of the copolymer chains.

In the ABP system, the predominant ordered phase is the lamellar (denoted as “L” in Fig. 4) for all particle radii, which stretches over roughly 25% of the available  $f_A$  range in the middle of the phase diagram. Particles are typically dispersed within the B-rich domains, in some circumstances

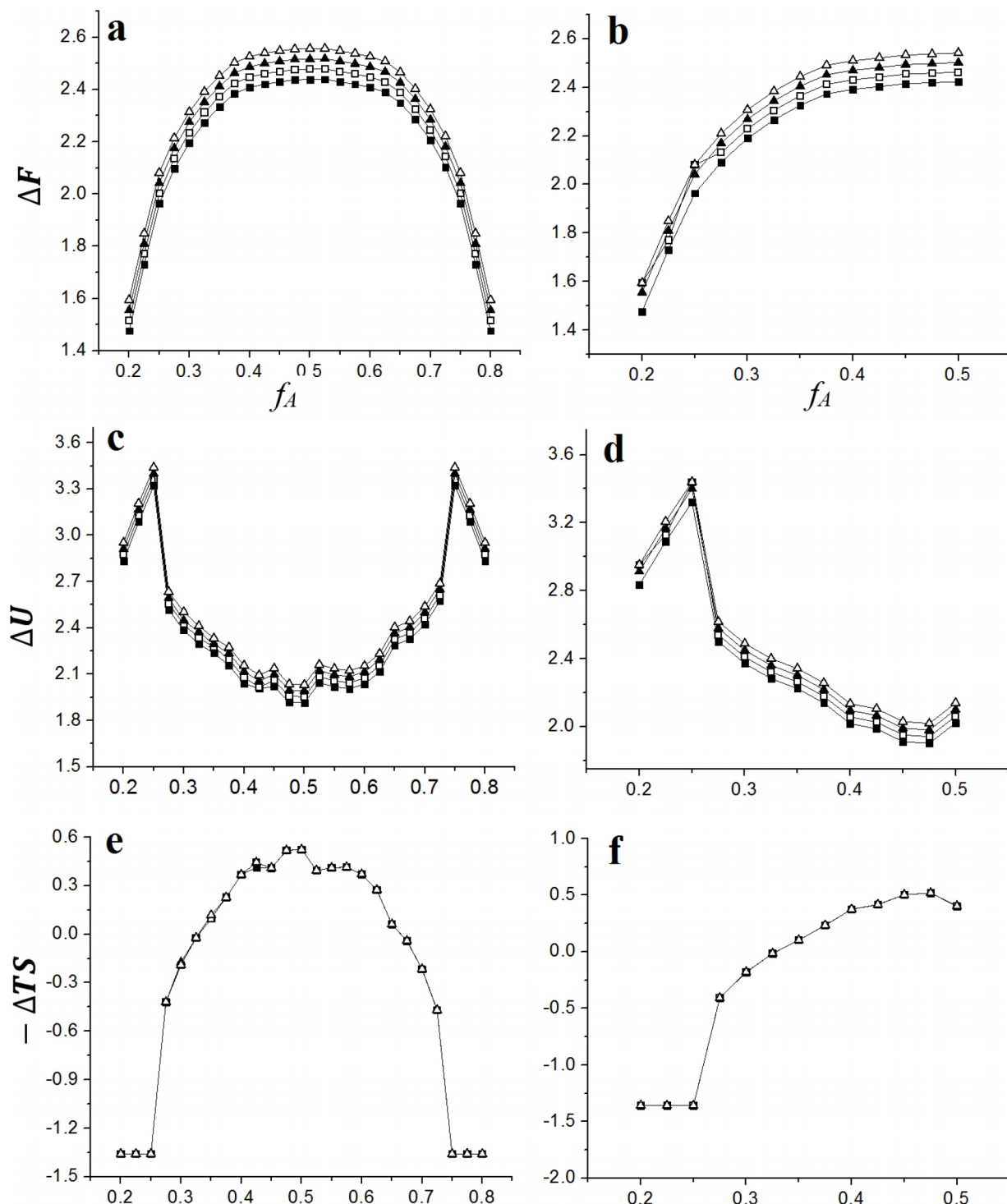


FIG. 3. The thermodynamic quantities as functions of  $f_A$  for repulsive particles of varying interaction potential strength, where  $\chi_{APN} = \chi_{BPN} \equiv \chi_{A/BP N} \geq 0$  at  $\chi_{ABN} = 18$  and  $R_P = 0.2R_g$ . The left column is the ABP system and the right column is the APB system. Symbols denote particles of a certain interaction energy as follows: ■ ( $\chi_{A/BP N} = 0$ ), □ ( $\chi_{A/BP N} = 5$ ), ▲ ( $\chi_{A/BP N} = 10$ ), and △ ( $\chi_{A/BP N} = 15$ ). Panels (a) and (b) depict the free energy change ( $\Delta F$ ), (c) and (d) show the internal energy change ( $\Delta U$ ), and (e) and (f) display the entropic change ( $-\Delta TS$ ).

tending to concentrate at the interfaces between the two types of domains. On either side of the lamellar region is a cylindrical phase (C), which consists of either B-rich cylinders arranged in a hexagonal packing pattern contained within an A-rich matrix phase (high  $f_A$ ) or vice versa (low  $f_A$ ). As observed previously, particles tend to disperse within the B-rich phase (at low  $f_A$ ) due to the tethering location but sometimes

congregate at the interface between the two phases (see Fig. 5). An interesting feature of these hexagonally packed cylinder domains is that at low  $f_A$ , the particles tend to concentrate in very small regions within the matrix phase, which are arranged symmetrically around the cylinder phase in a hexagonally packed array, forming cylindrical nanowire structures that parallel the cylindrical domains—see Fig. 5(a). At the low

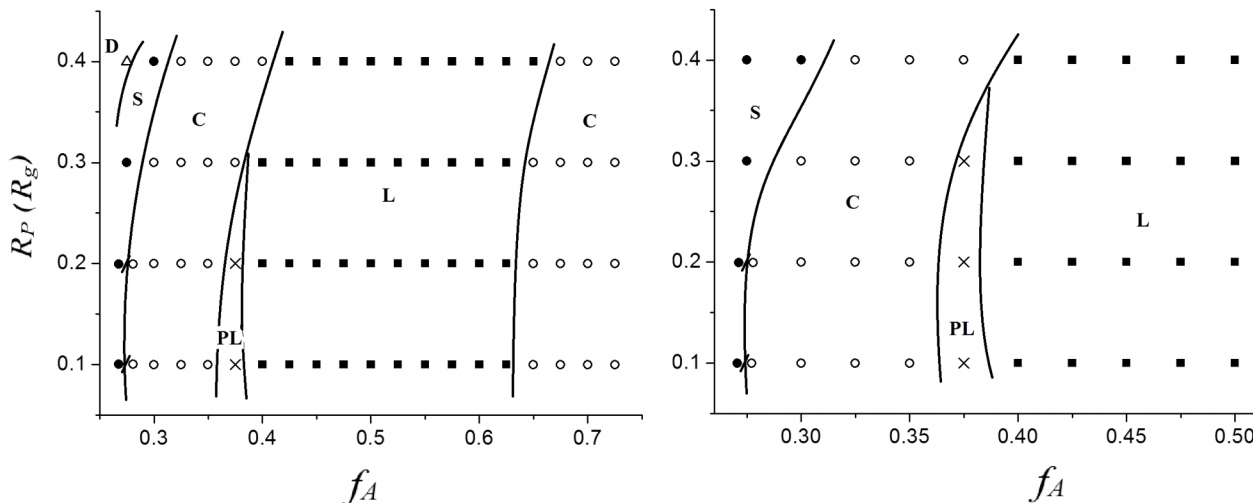


FIG. 4. Morphological phase diagrams of the ABP (left panel) and APB (right panel) systems as functions of  $f_A$  for different particle radii at  $\chi_{AB}N = 18$  and  $\chi_{A/BPN} = 0$ . The symbols in these diagrams denote various phases as follows: ■ lamellae (L), ○ cylinders (C), ● spheroids (S), •○ the cylinder/spheroid transition zone, × perforated lamellae (PL), and △ disordered (D).

and high extremes of the  $f_A$  range, ordered phases consisting of spheroids (S) arranged on body-centered cubic lattices are observed, with the particles concentrated within the B-rich spheroids or at the interfaces for high  $f_A$  values or within the B-rich matrix phase at low  $f_A$ . At the far extremes of the  $f_A$  range, disordered phases (D) still remain visible in the phase diagram. At low values of particle radii, there exists a small region of the phase diagram of Figure 4 where a PL morphology is the lowest free energy state (see Figure 6).

Regardless of particle diameter, the driving force behind the ordered-phase formation, and the particular ordered morphology that is formed, is the minimization of the overall free energy, which results from a delicate balance between the energetic effects which favor the ordering process and the entropic configurational effect which favors a disordered state. Ordered-phase formation is favorable to the free energy because it minimizes repulsive interactions between the A and B segments; however, this creates unnatural chain configurations (packing frustration) as the copolymer blocks contort to adjust to the spatial constraints forced on them by the geometry of the ordered phase. Consequently, which ordered morphology appears under a given circumstance is a strong function of  $f_A$  since this determines the number of A-B repulsive interactions: the more A-B interactions, the stronger the energetic effect contributes to the free energy, which leads to a higher possible degree of packing frustration imparted to the copolymer chains. Hence, a critical determiner of the particular ordered morphology formed for a specified value of  $f_A$  is the surface area to volume ratio; i.e., a large interfacial surface area allows for a higher energetic contribution to the free energy since more A and B segments can interact with each other, whereas a large volume (in the minority phase) results in a lower degree of chain packing frustration, which lowers the entropic contribution to the free energy. Therefore, as the overall average interfacial surface area to volume ratio (S/V) increases, the tendency is to drive the system morphology toward the disordered state. When  $f_A$  is approximately 0.5, there are relatively many A-B interactions,

and both blocks of the chain are fairly long. Hence, a large relative volume is required to relieve some of the packing frustration, while at the same time a relatively small surface area is required to minimize the A-B interactions as much as possible. These conditions favor the formation of the lamellar morphology. As  $f_A$  decreases, the B blocks become larger and the A blocks comprise the minority phase. Since the A blocks of the chains are shorter, they are able to pack into smaller volumes, thus allowing for geometric structures with greater surface areas, such as hexagonally arranged cylinders, to appear since the number of A-B interactions is lower simply because the number of A segments is lower. Further decrease in  $f_A$  allows the A blocks to pack into even smaller volumes with greater surface area, such as spheroids. At the extreme ends of the  $f_A$  range, the number of A-B interactions is so few, due to the shortness of one block or the other of the chain, that the configurational entropy dominates the free energy and the chains take on more natural configurations, producing the disordered phase.

The effect of particle radius on the phase diagram is remarkable. For very low radii, the effects of the particle are only slight, and the phase diagram is very similar quantitatively to that of the pure diblock copolymer system. The effect of increasing particle size is to drive the phase diagram transition zones inwards toward the mid-range of  $f_A$ . Since the larger particles impart a greater entropic contribution to the free energy than the smaller ones (as discussed in Secs. III A and III B), their net effect is to drive the system morphology toward a larger value of S/V at a constant value of  $f_A$ . In other words, the larger particles create a greater degree of packing frustration at a specific value of S/V, which implies a greater entropic contribution to the free energy.

The phase diagram of the APB system is very similar to that of the ABP system, except in this case the particles are almost always exclusively concentrated at the domain interfaces (see Fig. 5(c)), which is primarily a direct result of their tethering locations between the A and B blocks. Indeed, this is the major driving force behind the differences between

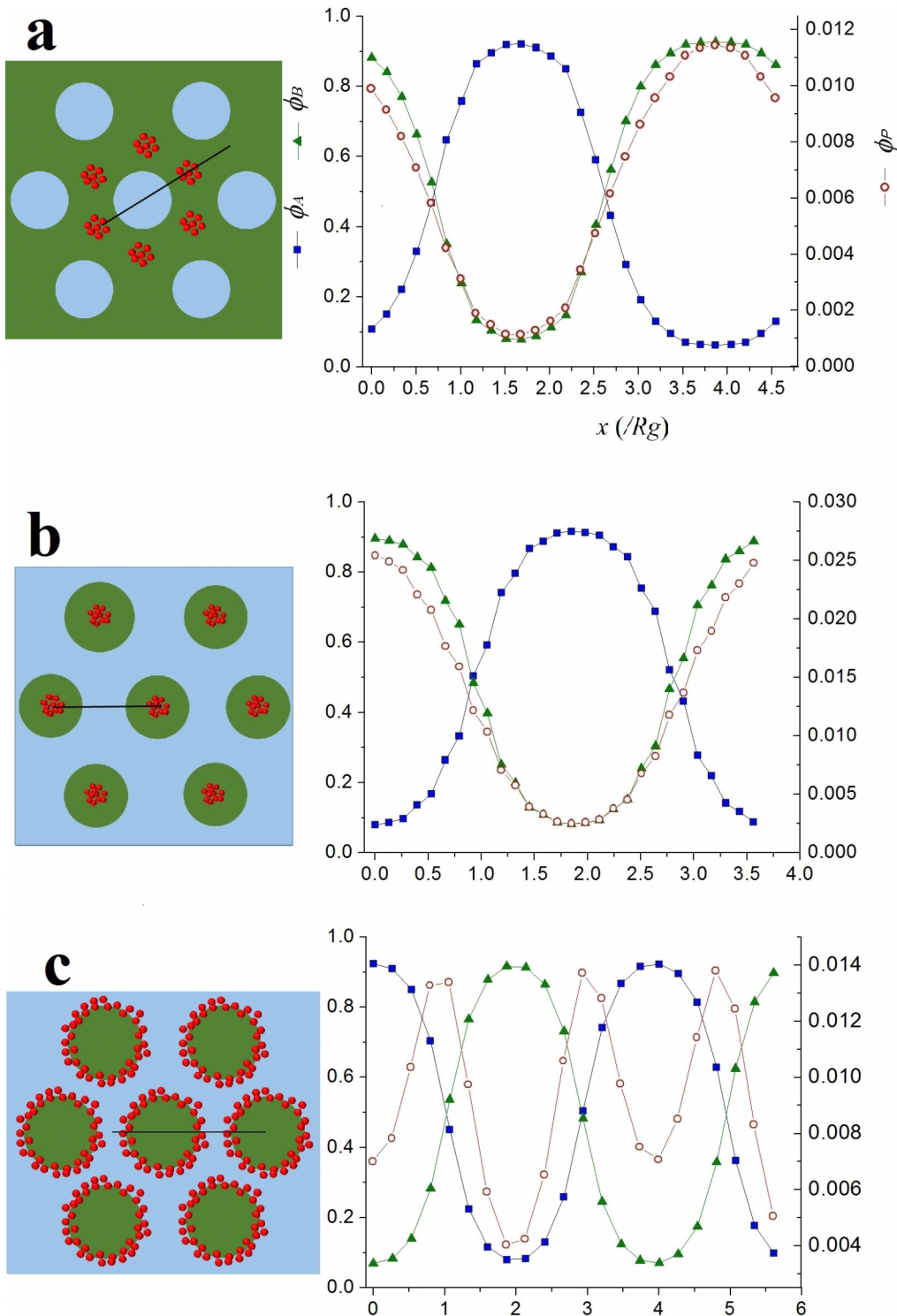


FIG. 5. Schematic morphology of the cylinder hexagonal packing configuration (left) and density distributions (right) at  $\chi_{AP}N = \chi_{BP}N = 0$ ,  $\chi_{AB}N = 18$ , and  $R_P = 0.2R_g$  corresponding to (a)  $f_A = 0.3$ , ABP system, (b)  $f_A = 0.7$ , ABP system, and (c)  $f_A = 0.3$ , APB system. The blue, green, and red colors represent the A-rich domains, the B-rich domains, and the primary regions of particle concentrations, respectively. The density distributions in the right panels are calculated over the spatial periods indicated in the left panels by the solid black lines.

the phase diagrams of the ABP and APB systems; i.e., the neutral particles serve to screen the A and B segments from each other, hence reducing the energetic contribution to the free energy. Consequently, at a specific value of  $f_A$ , the surface area of the APB system can be significantly smaller than that of the ABP system where the majority of particles are dispersed within the B-rich domains. Hence, the ratio S/V is smaller,

allowing for corresponding ordered phases to exist at lower (when  $f_A < 0.5$ ) and higher (when  $f_A > 0.5$ ) values of  $f_A$  in the APB system than in the ABP one.

The maxima in the particle density distributions, such as those in right-side panels of Fig. 5, are useful for quantifying the degree of relative concentration of particles at various locations within the ordered-phase morphology at  $\chi_{AB}N = 18$ .

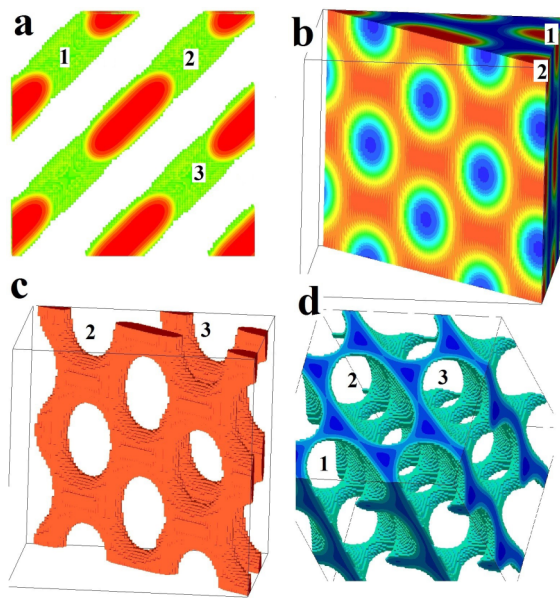


FIG. 6. Configuration of the PL phase for neutral particles in the ABP system at  $f_A = 0.375$ ,  $\chi_{AB}N = 18$ , and  $R_P = 0.2R_g$ . (a) The morphology of the A-block domain: 1, 2, and 3 are the layers formed by the A block. (b) A side view from layer 2 to layer 1 (blue represents the B-block domain). (c) The side view of the A-block domain (with  $\phi_A > 0.8$ ) from layer 2 to layer 3. (d) The B-block domain ( $\phi_B > 0.8$ ).

In Table II, we present data for the maximum particle density and the morphology wherein it appears in reference to Fig. 5 for neutral and interacting particles which disfavor both A and B segments for the ABP and APB systems. The symbol (a) denotes particles concentrated within hexagonally arrayed nanowires within the B-rich matrix phase, (b) corresponds to

TABLE II. Maximum particle densities ( $\phi_P^{\max}$ ) and observed morphology of the ABP and APB systems as functions of particle radius and interaction parameter at  $f_A = 0.3$  and  $\chi_{AB}N = 18$ . Numerical values correspond to  $\phi_P^{\max}$  whereas the letters denote the location of the particles with reference to the three cases of Fig. 5; i.e., (a) represents particles concentrated within hexagonally arrayed nanowires within the B-rich matrix phase, (b) corresponds to particles concentrated at the center of A-rich cylinders, and (c) denotes particles lining the interfaces between the B-rich matrix phase and the A-rich cylindrical domains. Note that (\*) and (\*\*) denote the spheroidal morphology, which assumes a body-centered cubic arrangement. Particles concentrate in the surrounding B-rich matrix in (\*), whereas they surround the A-rich spheroids in (\*\*).

		$\chi_{APN} = \chi_{BPN}$			
ABP	$R_P(R_g)$	0	5	10	15
0.1	0.0014 (a)	0.0014 (a)	0.0014 (a)	0.0014 (a)	
0.2	0.011 (a)	0.011 (a)	0.011 (a)	0.011 (a)	
0.3	0.034 (a)	0.034 (a)	0.034 (a)	0.034 (a)	
0.4	0.07 (*)	0.07 (*)	0.07 (*)	0.07 (*)	

		$\chi_{APN} = \chi_{BPN}$			
APB	$R_P(R_g)$	0	5	10	15
0.1	0.0018 (c)	0.0018 (c)	0.0018 (c)	0.0018 (c)	
0.2	0.013 (c)	0.013 (c)	0.013 (c)	0.013 (c)	
0.3	0.04 (c)	0.04 (c)	0.04 (c)	0.04 (c)	
0.4	0.08 (**)	0.08 (**)	0.08 (**)	0.08 (**)	

particles concentrated at the center of A-rich cylinders, and (c) denotes particles lining the interfaces between the B-rich matrix phase and the A-rich cylindrical domains. Additionally, the symbols (\*) and (\*\*) denote the spheroidal morphology, which assumes a body-centered cubic arrangement. Particles concentrate in the surrounding B-rich matrix in (\*), whereas they concentrate at the interfaces of the A-rich spheroids in (\*\*).

The maximum particle density increases substantially as the particle size increases in both the ABP and APB systems, indicating that the particles are more preferentially concentrated in certain locations within the phase morphology, although this is to some degree simply an expected consequence of the increase in the global average particle density,  $f_P$ , with particle size. A more interesting observation is that  $\phi_P^{\max}$  is independent of the particle/segment interaction strength for equally repulsive particles ( $\chi_{APN} = \chi_{BPN} > 0$ ); i.e., each value of interaction strength in Table II has the same value of  $\phi_P^{\max}$  as the neutral particle case. Although the particle/segment interactions can affect the critical point (see Table I), particularly at high particle radius, their effect on the maximum particle density is negligible, which is responsible for the common curve for the various entropy changes in Figs. 3(e) and 3(f). Because the particles are equally repulsive to both A and B segments, there is no net effect of internal energy on the configurational state of the copolymer chains; i.e., whatever so happens to be the most favorable entropic configurational state of the neutral particle system also is the most favorable state of an interacting particle system. Hence the particular morphology formed at a given value of  $\chi_{AB}N$  is independent of the interaction strength when the particles are equally repulsive to A and B segments.

Table III displays similar  $\phi_P^{\max}$  and morphology data as Table II for several different  $f_A$  phase points for the ABP and APB systems. These data exhibit the same trends as

TABLE III. Maximum particle density and the observed morphology for tethered particles as functions of particle radius and  $f_A$  for the ABP and APB systems at  $\chi_{AB}N = 18$ : (a) represents particles concentrated within hexagonally arrayed nanowires within the B-rich matrix phase, (b) corresponds to particles concentrated at the center of A-rich cylinders, and (c) denotes particles lining the interfaces between the B-rich matrix phase and the A-rich cylindrical domains. Particles concentrate in the surrounding B-rich matrix in (\*), whereas they surround the A-rich spheroids in (\*\*).

		$\phi_P^{\max}$			
		$R_P$ (for $\chi_{APN} = \chi_{BPN} = 0$ )			
System		0.1	0.2	0.3	0.4
ABP: $f_A = 0.3$	0.0014 (a)	0.011 (a)	0.034 (a)	0.07 (*)	
ABP: $f_A = 0.7$	0.0034 (b)	0.024 (b)	0.065 (b)	0.11 (b)	
APB: $f_A = 0.3$	0.0018 (c)	0.013 (c)	0.04 (c)	0.08 (**)	

		$\chi_{APN} = \chi_{BPN}$ (for $R_P = 0.2$ )			
System		0	5	10	15
ABP: $f_A = 0.3$	0.011 (a)	0.011 (a)	0.011 (a)	0.011 (a)	
ABP: $f_A = 0.7$	0.024 (b)	0.024 (b)	0.024 (b)	0.024 (b)	
APB: $f_A = 0.3$	0.013 (c)	0.013 (c)	0.013 (c)	0.013 (c)	

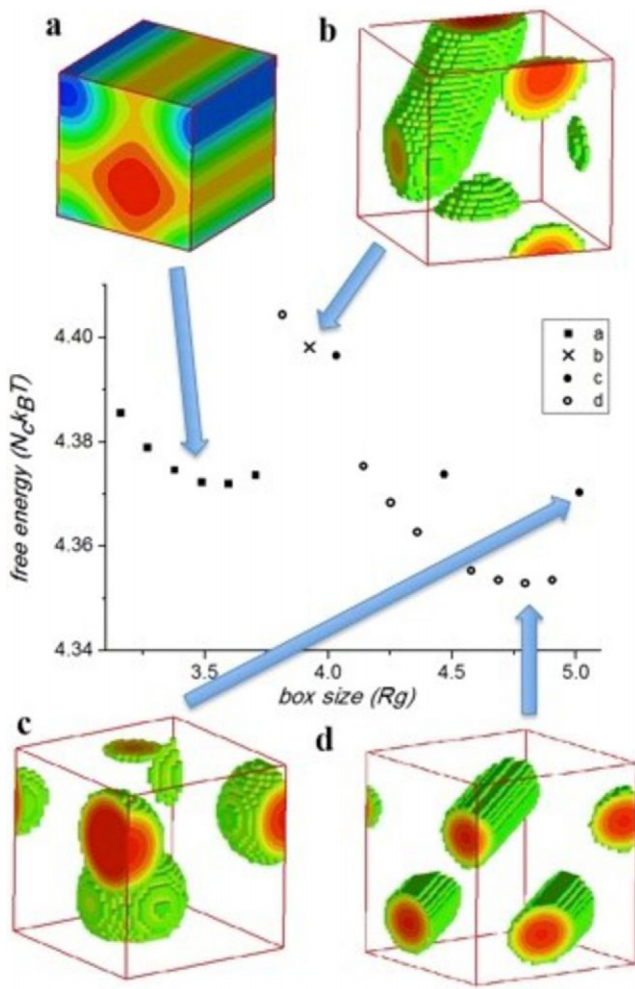


FIG. 7. The box size confinement effect on the free energy and the resulting morphologies for  $R_p = 0.2R_g$ ,  $\chi_{AB}N = 18$ ,  $\chi_{A/BPN} = 10$ , and  $f_A = 0.3$  of the ABP system. (a) Cylindrical domains in a quadrilateral array: the cylinders at the four corners (blue) are the A-block domains, and the red in the center is a particle nanowire; (b) ellipsoidal domains in quadrilateral arrays; (c) spheroids arranged on a body-centered cubic lattice; and (d) hexagonally packed cylinders (which were the globally stable phase). The (b)–(d) cells show only the shape of the A-block domain (green and red).

those of Table II but additionally illustrate the change in particle concentration that occurs as the particle tethering position changes and as the minority phase changes from A to B. Changing the tethering point of the particle at constant  $f_A = 0.3$  results in a movement of the particles from the bulk B-rich matrix phase to the interfaces between the A and B domains. As  $f_A$  is increased from 0.3 to 0.7 in the ABP system, the morphology switches from the A-rich cylindrical phase to a B-rich cylindrical phase, with a migration of the particles to the center of the cylinders and a commensurate dramatic increase in the particle concentration at the preferred location. Once again, there is no effect of particle/segment interaction strength on the position of the particles.

It is also interesting to study the effect of simulation box size on the observed morphology formed by the self-assembly of tethered-particle/copolymer materials. The constraint-free equilibrium morphology was always selected as that corresponding to the absolute minimum calculated value of the free energy, which was obtained by meticulously varying the

simulation box dimensions over wider ranges of multiples of the copolymer radius of gyration; however, in so doing, we noted that the stable morphology varied remarkably with box size. In Figure 7, we display various system morphologies obtained at one distinct set of parameter values,  $R_p = 0.2R_g$ ,  $\chi_{AB}N = 18$ ,  $\chi_{A/BPN} = 10$ , and  $f_A = 0.3$  of the ABP system. The four morphologies observed in relation to box size were (a) cylindrical minority phases arranged in quadrilateral arrays with particle-rich nanowires running axial-wise through the center of the interstice formed by four neighboring cylinders, (b) ellipsoidal domains arranged in quadrilateral arrays, (c) spheroids arranged on a body-centered cubic lattice, and (d) hexagonally packed cylinders (which were the globally stable phase). This illustrates clearly two points: (1) the effect of confinement to narrow dimensions upon the globally stable morphology induced by the self-assembly process and (2) the great care that must be taken to ascertain the globally stable morphology when performing SCFT/DFT simulations. According to (1), it is possible to influence the morphology of a BCP-NP system considerably by applying boundary constraints (such as solid surfaces) upon the self-assembly process. With regard to (2), it is evident from Fig. 7 that even in a constraint-free (unbounded) system, the global minimum in the free energy is not necessarily obtained in the limit of large box sizes; i.e., the appropriate box size must be chosen so as to conform to the natural periodicity of the most stable morphology or else unphysical configurations can be forced upon the block copolymer chains, resulting in morphologies that would not otherwise be globally stable under equilibrium conditions.

#### IV. CONCLUSIONS

In summary, particle size was shown to have a dramatic effect on the morphology and thermodynamics of both end-tethered and center-tethered particle/block copolymer systems. Increasing particle size raises the configurational entropy of the system, resulting in more disordered phases at equivalent values of the block length ( $f_A$ ) and A-B block interaction strength ( $\chi_{AB}N$ ). The particles generally congregate within the B-rich phase in the case of end-tethered particles or at the interfaces between the A and B domains in the case of center-tethered particles, although the particular morphology formed, spheroidal, lamellar, or cylindrical, is highly dependent on the value of  $f_A$ . The number of stable morphologies is reduced as particle radii increases, with the perforated lamellar morphology disappearing for particle radii larger than  $R_p = 0.3$ . Which particular morphology was formed under a specific circumstance was also highly dependent on the nature of the particles, i.e., how they interacted with the A and B copolymer segments. Thermodynamically, the particle radius has a dramatic effect on the configurational entropy of the system, but only a relatively weak effect on the internal energy. Hence, the free energy change that accompanies an increase in particle size is mostly due to its entropic contribution. The effect of particle size on the disorder/order phase transition was demonstrated to depend highly on the nature of the particles as well as the tethering point, with end-tethered particles displaying much larger variations in the critical value of  $\chi_{AB}N$ .

due to the impact of energetic screening by the particles located at the interfaces for center-tethered particle systems. Given these results, it is apparent that particle size can be a very important parameter when designing tethered-particle/block copolymer materials for many technical applications.

## ACKNOWLEDGMENTS

The authors would like to thank Dr. Xianggui Ye for his helpful criticism of this work. We also gratefully acknowledge the support of this work by the NSF-funded TN-SCORE program, NSF EPS-1004083, under Thrust 2. Computational resources were provided by the National Science Foundation under Grant No. CBET-0742679 to the PolyHub Virtual Organization.

- <sup>1</sup>T. A. Zawodzinski, T. E. Springer, F. Uribe, and S. Gottesfeld, "Characterization of polymer electrolytes for fuel cell applications," *Solid State Ionics* **60**, 199–211 (1993).
- <sup>2</sup>D. R. Morris and X. Sun, "Water-sorption and transport properties of Nafion 117 H," *J. Appl. Polym. Sci.* **50**, 1445–1452 (1993).
- <sup>3</sup>D. B. Spry and M. D. Fayer, "Proton transfer and proton concentrations in protonated Nafion fuel cell membranes," *J. Phys. Chem. B* **113**, 10210–10221 (2009).
- <sup>4</sup>J. Huh, V. V. Ginzburg, and A. C. Balazs, "Thermodynamic behavior of particle/diblock copolymer mixtures: Simulation and theory," *Macromolecules* **33**, 8085–8096 (2000).
- <sup>5</sup>T. B. Martin, A. Seifpour, and A. Jayaraman, "Assembly of copolymer functionalized nanoparticles: A Monte Carlo simulation study," *Soft Matter* **7**, 5952–5964 (2011).
- <sup>6</sup>M. K. Petersen and G. A. Voth, "Characterization of the solvation and transport of the hydrated proton in the perfluorosulfonic acid membrane Nafion," *J. Phys. Chem. B* **110**, 18594–18600 (2006).
- <sup>7</sup>S. Cui, J. Liu, M. Esai Selvan, D. J. Keffer, B. J. Edwards, and W. V. Steele, "A molecular dynamics study of a Nafion polyelectrolyte membrane and the aqueous phase structure for proton transport," *J. Phys. Chem. B* **111**, 2208–2219 (2007).
- <sup>8</sup>V. Pryamitsyn and V. Ganesan, "Strong segregation theory of block copolymer-nanoparticle composites," *Macromolecules* **39**, 8499–8510 (2006).
- <sup>9</sup>L. Meli, A. Arceo, and P. F. Green, "Control of the entropic interactions and phase behavior of athermal nanoparticle/homopolymer thin film mixtures," *Soft Matter* **5**, 533–537 (2009).
- <sup>10</sup>G. H. Fredrickson, *The Equilibrium Theory of Inhomogeneous Polymers* (Oxford University Press, Oxford, 2006).
- <sup>11</sup>F. Drolet and G. H. Fredrickson, "Combinatorial screening of complex block copolymer assembly with self-consistent field theory," *Phys. Rev. Lett.* **83**, 4317–4320 (1999).
- <sup>12</sup>F. Drolet and G. H. Fredrickson, "Optimizing chain bridging in complex block copolymers," *Macromolecules* **34**, 5317–5324 (2001).
- <sup>13</sup>S. W. Sides, B. J. Kim, E. J. Kramer, and G. H. Fredrickson, "Hybrid particle-field simulations of polymer nanocomposites," *Phys. Rev. Lett.* **96**, 250601 (2006).
- <sup>14</sup>Q. Y. Pan, C. H. Tong, and Y. J. Zhu, "Self-consistent-field and hybrid particle-field theory simulation of confined copolymer and nanoparticle mixtures," *ACS Nano* **5**, 123–128 (2011).
- <sup>15</sup>M. W. Matsen and F. S. Bates, "Origins of complex self-assembly in block copolymers," *Macromolecules* **29**, 7641–7644 (1996).
- <sup>16</sup>M. W. Matsen and F. S. Bates, "Unifying weak- and strong-segregation block copolymer theories," *Macromolecules* **29**, 1091–1098 (1996).
- <sup>17</sup>M. W. Matsen and F. S. Bates, "Block copolymer microstructures in the intermediate-segregation regime," *J. Chem. Phys.* **106**, 2436–2448 (1997).
- <sup>18</sup>K. C. Daoulas, M. Muller, M. P. Stoykovich, S. M. Park, Y. J. Papakonstantopoulos, J. J. de Pablo, P. F. Nealy, and H. H. Solak, "Fabrication of complex three-dimensional nanostructures from self-assembling block copolymer materials on two-dimensional chemically patterned templates with mismatched symmetry," *Phys. Rev. Lett.* **96**, 036104 (2006).
- <sup>19</sup>X. Ye, B. J. Edwards, and B. Khomami, "Elucidating the formation of block copolymer nanostructures on patterned surfaces: A self-consistent field theory study," *Macromolecules* **43**, 9594–9597 (2010).
- <sup>20</sup>X. Ye, B. J. Edwards, and B. Khomami, "Morphology tailoring of thin film block copolymers on patterned substrates," *Macromol. Rapid Commun.* **33**, 392–395 (2012).
- <sup>21</sup>X. Ye, B. J. Edwards, and B. Khomami, "Block copolymer morphology formation on topographically complex surfaces: A self-consistent field theoretic study," *Macromol. Rapid Commun.* **35**, 702–707 (2014).
- <sup>22</sup>J. Y. Choi, T. Takayama, H. C. Yu, C. M. Chung, and K. Kudo, "Preparation and characterization of nanoporous films derived from alicyclic copolyimides having pendent poly(propylene glycol) groups," *Polymer* **53**, 1328–1338 (2012).
- <sup>23</sup>T. Hirai, M. Leolukman, C. C. Liu, E. Han, Y. J. Kim, Y. Ishida, T. Hayakawa, M. Kakimoto, P. F. Nealey, and P. Gopalan, "One-step direct-patterning template utilizing self-assembly of POSS-containing block copolymers," *Adv. Mater.* **21**, 4334 (2009).
- <sup>24</sup>G. Decher and J. D. Hong, "Buildup of ultrathin multilayer films by a self-assembly process. 1. Consecutive adsorption of anionic and cationic bipolar amphiphiles on charged surfaces," *Makromol. Chem., Macromol. Symp.* **46**, 321–327 (1991).
- <sup>25</sup>M. Doi, *Introduction to Polymer Physics* (Clarendon Press, Oxford, 2001).
- <sup>26</sup>B. Sarkar and P. Alexandridis, "Self-assembled block copolymer-nanoparticle hybrids: Interplay between enthalpy and entropy," *Langmuir* **28**, 15975–15986 (2012).
- <sup>27</sup>Q. Wang, P. F. Nealey, and J. J. de Pablo, "Behavior of single nanoparticle/homopolymer chain in ordered structures of diblock copolymers," *J. Chem. Phys.* **118**, 11278–11285 (2003).
- <sup>28</sup>R. B. Thompson, V. V. Ginzburg, M. W. Matsen, and A. C. Balazs, "Predicting the mesophases of copolymer-nanoparticle composites," *Science* **292**, 2469–2472 (2001).
- <sup>29</sup>R. B. Thompson, V. V. Ginzburg, M. W. Matsen, and A. C. Balazs, "Block copolymer-directed assembly of nanoparticles: Forming mesoscopically ordered hybrid materials," *Macromolecules* **35**, 1060–1071 (2002).
- <sup>30</sup>L. Zhang, J. Lin, and S. Lin, "Self-assembly behavior of amphiphilic block copolymer/nanoparticle mixture in dilute solution studied by self-consistent-field theory/density functional theory," *Macromolecules* **40**, 5582–5592 (2007).
- <sup>31</sup>D. Trombly and V. Ganesan, "Interactions between polymer-grafted particles and bare particles for biocompatibility applications," *J. Polym. Sci., Part B: Polym. Phys.* **47**, 2566–2577 (2009).
- <sup>32</sup>E. R. Chan, L. C. Ho, and S. C. Glotzer, "Computer simulations of block copolymer tethered nanoparticle self-assembly," *J. Chem. Phys.* **125**, 064905 (2006).
- <sup>33</sup>G. K. Xu and X. Q. Feng, "Position transitions of polymer-grafted nanoparticles in diblock-copolymer nanocomposites," *Express Polym. Lett.* **5**, 374–383 (2011).
- <sup>34</sup>X. M. Zhu, L. Q. Wang, J. P. Lin, and L. S. Zhang, "Ordered nanostructures self-assembled from block copolymer tethered nanoparticles," *ACS Nano* **4**, 4979–4988 (2010).
- <sup>35</sup>B. Zhang, X. Ye, and B. J. Edwards, "A self-consistent field study of diblock copolymer/charged particle system morphologies for nanofiltration membranes," *J. Chem. Phys.* **139**, 244909 (2013).
- <sup>36</sup>J. J. Schwab and J. D. Lichtenhan, "Polyhedral oligomeric silsesquioxane (POSS)-based polymers," *Appl. Organomet. Chem.* **12**, 707–713 (1998).
- <sup>37</sup>H. Yockell-Lelievre, J. Desbiens, and A. M. Ritcey, "Two-dimensional self-organization of polystyrene-capped gold nanoparticles," *Langmuir* **23**, 2843–2850 (2007).
- <sup>38</sup>N. F. Carnahan and K. E. Starling, "Equation of state for nonattracting rigid spheres," *J. Chem. Phys.* **51**, 635–636 (1969).
- <sup>39</sup>K. Johnston and V. Harmandaris, "Hierarchical simulations of hybrid polymer-solid materials," *Soft Matter* **9**, 6696–6710 (2013).
- <sup>40</sup>V. V. Ginzburg, "Polymer-grafted nanoparticles in polymer melts: Modeling using the combined SCFT-DFT approach," *Macromolecules* **46**, 9798–9805 (2013).
- <sup>41</sup>D. W. Peaceman and H. H. Rachford, "The numerical solution of parabolic and elliptic differential equations," *J. Soc. Ind. Appl. Math.* **3**, 28–41 (1955).
- <sup>42</sup>R. B. Thompson, K. O. Rasmussen, and T. Lookman, "Improved convergence in block copolymer self-consistent field theory by Anderson mixing," *J. Chem. Phys.* **120**, 31–34 (2004).
- <sup>43</sup>L. Leibler, "Theory of microphase separation in block copolymers," *Macromolecules* **13**, 1602–1617 (1980).
- <sup>44</sup>G. H. Fredrickson and E. Helfand, "Fluctuation effects in the theory of microphase separation in block copolymers," *J. Chem. Phys.* **87**, 697–705 (1987).
- <sup>45</sup>J. F. Marko, "Microphase separation of block copolymer rings," *Macromolecules* **26**, 1442–1444 (1993).